

**Title:**

Seismicity associated with magmatism, faulting and hydrothermal circulation at Aluto Volcano, Main Ethiopian Rift.

**Authors:**

Matthew Wilks<sup>a1</sup>, J-Michael Kendall<sup>a</sup>, Andy Nowacki<sup>b</sup>, Juliet Biggs<sup>a</sup>, James Wookey<sup>a</sup>, Yelebe Birhanu<sup>a</sup>, Atalay Ayele<sup>c</sup> & Tulu Bedada<sup>c</sup>.

**Affiliations:**

a. School of Earth Sciences, University of Bristol, Wills Memorial Building, Queens Road, Bristol, UK. BS8 1RJ.

b. School of Earth and Environment, University of Leeds, Leeds, UK. LS2 9JT.

c. Institute of Geophysics, Space Science, and Astronomy, Addis Ababa University, Addis Ababa, Ethiopia.

**Present Address**

1. NORSAR, Gunnar Randers vei 15, 2007 Kjeller, Norway.

**Corresponding Author:**

Matthew Wilks

Email: matt@norsar.no

Tel: +47 47 504039

**Abbreviated Title:**

Magmatic, Tectonic and Geothermal Seismicity at Aluto

## 1. Abstract

The silicic volcanic centres of the Main Ethiopian Rift (MER) play a central role in facilitating continental rifting. Many of these volcanoes host geothermal resources and are located in heavily populated regions. InSAR studies have shown several are deforming, but regional seismic networks have detected little seismicity. A local network of 12 seismometers was deployed at Aluto Volcano from 2012–2014, and detected 2142 earthquakes within a 24-month period. We locate the events using a 1D velocity model that exploits a regional model and information from geothermal boreholes and calculate local magnitudes, b-values and focal mechanisms. Event depths generally range from the near surface to 15 km with most of the seismicity clustering in the upper 2 km. A significant amount of seismicity follows the Artu Jawa Fault Zone, which trends in alignment with the Wonji Fault Belt, NNE–SSW and is consistent with previous studies of strain localisation in the MER. Focal mechanisms are mostly normal in style, with the mean T-axes congruent to the orientation of extension in the rift at this latitude. Some show relatively small left-lateral strike-slip components and are likely associated with the reactivation of NE-ENE structures at the southern tip of the Aluto-Gedemsa segment. Events range from -0.40 to 2.98 in magnitude and we calculate an overall b-value of  $1.40 \pm 0.14$ . This relatively elevated value suggests fluid-induced seismicity that is particularly evident in the shallow hydrothermal reservoir and above it. Subdividing our observations according to depth identifies distinct regions beneath the volcanic edifice: a shallow zone (-2–0 km) of high seismicity and high b-values that corresponds to the hydrothermal system and is influenced by a high fluid saturation and circulation; a relatively aseismic zone (0–2 km) with low b-values that is impermeable to ascending volatiles; a region of increased fluid-induced seismicity (2–9 km) that is driven by magmatic intrusion from below and a deeper zone (below 9 km) that is interpreted as a partially crystalline, magmatic mush. These observations indicate that both the magmatic and hydrothermal systems of Aluto volcano are seismically active and highlights the need for dedicated seismic monitoring at volcanoes in the MER.

**Key Words:** Hydrothermal Systems, Seismicity and Tectonics, Volcano Seismology, Volcano Monitoring, Africa, Continental Tectonics: extensional.

## 2. Introduction

The East African Rift captures the transition from continental rifting to oceanic spreading, providing opportunities to study the extensional processes that lead to the formation of new oceanic basins (Chorowicz 2005). Spanning embryonic rifting in the Okavango (Southwestern rift) and southwestern Mozambique (Western rift) regions to the south (Yang and Chen, 2008; Ebinger and Scholz, 2012) to mature spreading around the Afar Triple Junction in the north, the intermediate stages of the progression are exposed at the surface of the Main Ethiopian Rift (MER) (Fig. 1), where magmatic processes have played a central role in facilitating lithospheric thinning since  $\sim 2$  Ma (Ebinger and Casey 2001). As a consequence of this focusing of extensional strain to zones of dike intrusion and magma storage at the rift's centre, widespread magmatism has produced a new along-axis segmentation along the length of the rift. Numerous silicic caldera-bearing volcanoes have since developed within these segments and at their offsets (Mohr 1962; WoldeGabriel et al. 1990).

Although an increasing number of geophysical, including seismic, studies have been conducted in the MER over the past decades, the majority have focused their attention towards latitudes north of  $8^{\circ}\text{N}$  and on the Afar region (e.g., Hofstetter and Beyth 2003; Casey et al. 2006; Maguire et al. 2006; Daly et al. 2008). In contrast, the volcanoes of the MER have received little-to-no individual seismic monitoring, which is significant, as volcanic and seismic hazard remain relatively poorly

constrained (Wilks et al. 2017). This is despite many of these volcanoes being volcanically active in the Holocene and many continuing to show significant unrest at the surface (Biggs et al. 2011).

Situated between Lakes Ziway to the north and Langano to the south, Aluto is one example of a MER volcano where geophysical monitoring has remained largely absent (Fig. 1). However, satellite observations of surface deformation have been made via Interferometric Synthetic Aperture Radar (InSAR) and revealed multiple episodes of uplift and subsidence of up to 15 cm in displacement (Biggs et al. 2011). At Aluto, these deformation episodes are interpreted to represent the repeated injection of magmatic fluids and volatiles to shallow (<5 km) depths driving inflation and the cooling and flow of hydrothermal fluids causing subsequent subsidence (Hutchison et al. 2016).

With the hypothesis that the replenishment of subsurface magma bodies can drive structurally controlled geothermal systems (Hill et al. 1985; Moore et al. 2008), fluid migration at high temperature has the potential to provide an abundant renewable energy resource. For this reason, geothermal power has gained significant interest in the MER, with Aluto in particular being identified as a promising field for the generation of renewable energy. Explorational drilling in the 1980s revealed temperatures of ~350 °C at 2.5 km depth, indicating the influence of hot subsurface magmatic bodies in the shallow crust (Gizaw, 1993; Gianelli and Teklemariam 1993) and also Aluto's potential as a viable energy resource. Ethiopia's first geothermal power plant (the Aluto-Langano Geothermal Plant) was consequently constructed in 1999 (Teklemariam and Beyene 2002) with expansion from a generating capacity of 7.3 MW to 70 MW beginning in late-2013 and continuing today.

The MER has long been recognised as a seismically active region and many earthquakes have had structurally damaging consequences (Gouin 1979). Due to the scarcity of station coverage in Ethiopia during most of the 20th century however, constraining seismic source parameters and quantifying the associated hazard has not been possible until recently (e.g., Foster and Jackson 1998; Ayele et al. 2007; Belachew et al. 2012). Earthquakes of low-to-intermediate ( $M < 6$ ) magnitudes occurring in relatively diffuse patterns across the rift axis characterises the seismicity of the MER, although a maximum expected magnitude of ~7 has also been estimated (Hofstetter and Beyth 2003). At the latitude of Aluto, the seismic hazard is thought to be less than to the north and south of it (Midzi et al. 1999; Grünthal et al. 1999) but the  $M_w$  5.3 earthquake on 27<sup>th</sup> January 2017 that occurred ~70 km from Aluto (Fig. 1) serves as an example that the risk of ground motions on a damaging scale persist. At volcanoes, volcanic unrest is often complimented by profuse seismicity that reflects activity within the hydrothermal-magmatic system. Therefore it is extremely important to monitor earthquakes where deformation has been observed to develop our understanding of these processes, which becomes of further relevance when economic interest for power generation is also associated. In a region where the local population is also rapidly increasing, these factors suggest that monitoring at volcanoes such as Aluto should be improved (Sparks et al. 2012).

In this paper we aim to better understand the hydrothermal-magmatic interactions at an actively deforming volcano where geophysical monitoring has remained relatively sparse. This study of the microseismicity around Aluto constitutes one component of the Aluto Research and Geophysical Observations (ARGOS) project, which is a multi-disciplinary project integrating InSAR, GPS, magnetotellurics (MT), CO<sub>2</sub> degassing experiments and geological mapping data to place quantitative constraints on the causes of unrest for the first time (Hutchison et al. 2015a, Hutchison et al. 2015b; Samrock et al. 2015).

We present the seismicity around Aluto with data acquired from passive seismic monitoring over a two-year period. Firstly, we locate earthquakes using a 1D seismic velocity model and examine them spatially and temporally. We compute local magnitudes using an empirical relation that

accounts for attenuation in the Main Ethiopian Rift (Keir et al. 2006b) and investigate their distributions with respect to the Gutenberg-Richter relationship. We then calculate source mechanisms for a subset of the earthquake catalogue to investigate faulting and the subsurface stress-state and finally combine these observations to produce a model to describe our interpretations of the hydrothermal-magmatic system.

### 3. The Main Ethiopian Rift and Volcanism at Aluto

The Central MER (CMER) is bounded by large, ~50 km-long, widely-spaced border faults that formed during the primitive stages of rifting 8–6 Ma (WoldeGabriel et al. 1990; Bonini et al. 2005) and whose mean trend is at N032°E at this latitude (Agostini et al. 2011) (Fig. 1). Early rifting during this time was complimented by widespread bimodal volcanism, with large ignimbritic eruptions occurring at Munesa at 3.5 Ma (WoldeGabriel et al. 1990) and at Gademotta, which last erupted at 1.3 Ma (Laury and Albritton 1975) for example (Fig. 2). Extension was facilitated by the border faults for the remainder of the Miocene, the Pliocene and into the Pleistocene but at 2 Ma, there was a drastic shift in rifting style where strain localised at the centre of the rift (Boccaletti et al. 1998; Ebinger and Casey 2001; Keir et al. 2015). Concentrated episodes of mafic magmatic intrusion, diking and faulting led to the formation of shorter (~20 km-long), NNE-SSW (~N012°E) trending faults that formed a dense series of right-stepping en-echelon structures (Keir et al. 2006a; Pizzi et al. 2006). The development of these internal rift faults, called the Wonji Fault Belt (WFB) coincided with basaltic fissure eruptions at the surface and produced the Bofa basalt sequence to overlie the ignimbrites below (Kebede et al. 1985; ELC Electroconsult 1986).

Widespread flooding of the evolving Ziway-Shala basin at 570 ka led to the deposition of clay-rich, lacustrine sediments, which continued until 330 ka (Le Turdu et al. 1999). This sedimentation was interspersed with the first silicic deposits in the area of trachytic tuffs and lavas, eruptive products that mark the onset of the formation of the Aluto complex (Hutchison et al. 2015b). As silicic deposits accumulated, the Aluto volcanic centre continued to grow until ~310 ka, when an explosive eruption(s) occurred (Hutchison et al. 2015a) and formed welded ignimbrites that are thickest at Aluto's centre (Dakin and Gibson 1974). At present, only the eastern rim of the caldera is preserved, with the western portion inferred from the alignment of volcanic centres and craters (Kebede et al. 1985).

A period of volcanic quiescence followed for ~240 ka at Aluto, in which time other caldera forming events occurred in the MER to the south at Shala (O'a caldera) and then Corbett (Mohr et al. 1980; Hutchison 2015). Post-caldera volcanism recommenced within the main edifice of Aluto at ~60 ka through rhyolitic lava flows, pumice fallouts and pyroclastic density currents. These eruptions produced distinct sequences that continued until at least 10 ka, perhaps until 2 ka (ELC Electroconsult 1986; Gianelli and Teklemariam, 1993), and are separated by palaeosols that indicate when volcanism temporarily ceased (Hutchison et al. 2015b).

Oxygen isotope measurements have shown that the majority (90%) of fluids within Aluto's geothermal system are derived from rainfall falling on the rift shoulders to the east (Darling et al. 1996). This observation, along with geochemical evidence that geothermal fluids interact with rhyolitic volcanic products (Gianelli and Teklemariam 1993) and the known temperatures and stratigraphy within deep exploration wells (Gizaw 1993; Teklemariam et al. 1996) suggest that the geothermal reservoir resides in the Neogene ignimbrite unit, which is the lowermost and oldest unit in the geothermal wells (Teklemariam et al. 1996). The low porosity and low permeability lake-derived sediments then act as a 'clay cap' to seal the reservoir, which have experienced intense hydrothermal alteration (Teklemariam et al. 1996) and have been imaged by MT surveying (Samrock et al. 2015).

Although the majority of strain in the CMER has been accommodated by the WFB since  $\sim$ 2 Ma, the majority of the mapped fault structures around Aluto and particularly to the east, are the older and relatively inactive border faults (Agostini et al. 2011) (Fig. 3). Within and around the Aluto edifice however, short lineaments trending NNE-SSW and following the trend of the WFB have been identified (Kebede et al. 1985). These include a fault scarp that cross-cuts the main edifice of Aluto in the same orientation called the Artu Jawa Fault Zone (AJFZ) (Hutchison et al. 2015a). This structure has been identified as the primary pathway along which hydrothermal fluids and gases (steam and CO<sub>2</sub>) ascend from the geothermal reservoir to the surface and is where the productive geothermal wells are located.

## 4. Methods

### 4.1. Seismic Network and Data

To monitor the seismicity around Aluto, a seismic network of 12 Gürnalp CMG-6TD three-component seismometers with a low corner of 30 s were deployed in January 2012. The stations were installed both within the volcanic edifice and encircling it, with stations also deployed on the surrounding rift valley floor and towards the eastern rift escarpment (Fig. 3). Station spacings were between 2 and 10 km and the array covered an area of  $20 \times 20$  km. A sampling rate of 100 Hz was maintained throughout the experiment and the instruments remained in the field until 30th January 2014. Two stations at A06E and A02E were relocated during the deployment (to become A13E and A14E respectively) due to noise and logistical considerations. A maximum of eleven stations were recording data at any one time but the network geometry provided good coverage of the seismicity beneath Aluto and provided a rich seismic dataset for analysis. Five GPS stations were also deployed around the volcano as part of the wider ARGOS project.

### 4.2. Event Detection and Locations

P- and S-wave arrivals are picked manually on seismograms using the Seismic Analysis Code (Goldstein and Snock 2005; Helffrich et al. 2013). A Butterworth bandpass filter of high and low corners of 15 and 2 Hz is applied to enhance the clarity of the arrivals and P-wave arrival picks are made where coherent first-breaks are observed at a minimum of 3 stations. P-wave onsets are initially identified on the vertical component of the seismograms, with all three components subsequently used to refine the picks and identify S-wave arrivals. The picks are manually attributed weightings to reflect their quality and clarity with assigned values of 0, denoting the highest quality, to 3, the lowest. The values are then mapped to P-wave arrival time uncertainties of 0.05, 0.1, 0.2 and 0.5 s and to S-wave uncertainties of 0.1, 0.2, 0.3 and 0.5 s. These errors are based on a semi-quantitative scale, where if inspection of the seismogram led to confidence in the pick to within  $\pm 0.05$  s (due to noise, an emergent onset, etc.), it was assigned a quality of '0', and so forth. Experience and the sampling rate also guided these values.

The determination of earthquake parameters such as locations and focal mechanisms is highly dependent on an accurate seismic velocity model. This can become particularly difficult in regions with significant topographic relief such as around volcanic edifices. Well-log records acquired from industrial drilling are used to constrain seismic velocities from the surface to a depth of 300 m below sea level (b.s.l.) (ELC Electroconsult 1986; Gizaw 1993; Gianelli and Teklemariam 1993; Teklemariam et al. 1996). The lithologies of the logs are mapped to the appropriate seismic velocity (Press 1966; Christensen 1984) to construct the top  $\sim$ 3 km of a 1D layer-cake model. At greater depths the velocity structure is taken from a passive source tomographic inversion that was determined using local earthquakes in the northern MER (Daly et al. 2008). The two velocity structures are then amalgamated to produce the 1D velocity model presented in Table 1.

Depth (km)	$V_P$ (km/s)	$V_S$ (km/s)	$\rho$ (kg/m <sup>3</sup> )	Geology
-2.5	3.27	1.88	2380	Silicic Volc.
-1.5	4.12	2.41	2380	Seds. & Tuffs
-1.0	4.22	2.49	2500	Bofa Basalt
-0.2	4.50	2.50	2500	Ignimbrite
0.3	4.62	2.58	2790	Crystalline Basement
2.0	4.70	2.58	2790	
4.0	4.95	2.77	2790	
6.0	5.12	2.78	2790	
8.0	5.85	3.36	2790	
10.0	5.99	3.53	2790	
12.0	6.09	3.61	2970	
14.0	6.26	3.61	2970	
16.0	6.31	3.61	2790	
20.0	6.35	3.68	2790	
25.0	6.70	3.80	2940	Lower Crust
30.0	6.89	3.92	2940	
40.0	7.50	4.28	3190	Upper Mantle

**Table 1:** The input P- and S-wave velocity model inferred from well-log data and a tomographic inversion in the northern MER. The reference depth at 0 km is sea level. Densities are derived from Cornwell et al. (2006). The inferred geologies are denoted in the right-hand column with the units derived from the well-logs coloured as in Fig. 2.

Arrival times are used as input to the earthquake hypocentre location software package *NONLINLOC* (Lomax et al. 2000) to perform a nonlinear global-search to attain absolute earthquake locations. The inversion follows the probabilistic approach of Tarantola and Valette (1982) and Tarantola (2005) to solve for the hypocentral location of maximum likelihood in time and space, which is represented by an a posteriori probability density function of model parameters. First, synthetic traveltimes from each station to every grid node of a 3D model grid are computed using a Huygen's principle finite-difference eikonal solver (Podvin and Lecomte 1991). In this approach, the variable topography of the study region is accounted for by first shifting the model space vertically by 2 km (the highest station is at 1955 m elevation). An oct-tree 3D importance sampling method is then implemented within *NONLINLOC*, which recursively subdivides grid cells to determine the location PDFs and hypocentres of maximum likelihood in an efficient and robust manner (Lomax and Curtis 2001; Lomax 2005).

### 4.3. Magnitudes

#### 4.3.1. Local Magnitude Scale

In seismically active zones it is essential to implement an objective and quantitative method of estimating the size of an earthquake. We use a local magnitude ( $M_L$ ) scale consisting of an attenuation term specific to the MER that is formulated as:  $M_L = \log(A_{WA}) + 1.196997 \log(r/17) + 0.001066(r - 17) + 2.0$ , where  $A_{WA}$  is the zero-to-peak displacement amplitude of the horizontal components on a Wood-Anderson seismograph in mm and  $r$  is the hypocentral distance in km (Keir et al. 2006b).

The instrument responses from the horizontal components of seismograms are removed and convolved to that of a Wood-Anderson instrument. Since maximum amplitude deflections are most

associated with S-waves for local events, amplitudes are measured in a time window encapsulating the onset of the S-wave arrival. For a single event the computed magnitudes across a network should theoretically be equal but variations in radiation patterns, station noise and local geology can amplify or diminish the signal at a particular station (Savage and Anderson 1995). We consequently apply station corrections by finding the magnitude residuals, which are defined as the difference between the calculated and average event magnitudes for each component and at each station. The arithmetic mean is then taken across each component at each station for all events and produces corrections ranging from  $-0.284$  and  $0.218$   $M_L$  units. Through the addition of the corrections the variance of the magnitude residuals is reduced by 22.4% from 0.092 to 0.072. Once the station corrections have been applied, we average the two magnitude values at each station to attain a single value that defines the  $M_L$ . The precision of the determined magnitudes is constrained by the uncertainty, which is the standard deviation of the variation in magnitudes that is computed at each station.

#### 4.3.2. b-Values

The Gutenberg-Richter relationship, which is defined as:  $N(M) = 10^{a-bM}$ , describes the distribution of earthquakes in a given region and timeframe with respect to the magnitude  $M$  (Gutenberg and Richter 1942).  $N$  is the number of earthquakes of magnitude greater than or equal to  $M$  and  $a$  and  $b$  are positive constants.  $a$  describes the seismic activity and is determined by the event rate, whereas  $b$  (termed the b-value) is a tectonic parameter that describes the relative abundance of large to small magnitude events. We use the maximum-likelihood method of Aki (1965) and Utsu (1965) to find  $b$  and also calculate the minimum magnitude of completeness ( $M_c$ ), which is defined as the minimum event magnitude at which the earthquake catalogue is assumed to contain all events. This is performed automatically using Kolmogorov-Smirnov tests to choose the smallest magnitude at which the similarity between the data curve (magnitude distribution) and the straight line fit (of gradient  $-b$ ) reaches a predetermined significance level (Kagan 1995). There is therefore no requirement to restrict the earthquake catalogue to events above  $M_c$  in the subsequent calculation of  $b$ .

#### 4.4. Focal Mechanisms

Calculating focal mechanisms is useful for characterising the seismicity of a region as they aid in determining the orientation of stress that leads to rupture and can help to infer the style of faulting. Here, double-couple source mechanisms are assumed (Belachew et al. 2012) and are derived from P- and SH-wave first-motion polarities and amplitude ratios using *FOCMEC* (Snoke et al. 1984), which systematically searches the focal sphere for acceptable orientations of the nodal planes. We select events that are recorded at a minimum of 6 stations with arrival time pick weights of 0 or 1 and that have a maximum azimuthal gap of  $180^\circ$ . We allow zero P-polarity errors and a maximum of one error in the SH-polarity.

We choose to use information from SH-wave polarities and amplitude ratios in addition to P-wave polarities. P-wave first motions are picked on the vertical component of the traces and SH-polarities are picked on the transverse components. This is performed on seismograms convolved to velocity but with no further processing in order to negate processing artefacts. Particular care is taken when picking S-wave polarities as they are more sensitive to local structure (Snoke 2003). For this reason SV-polarities are not considered as they are more prone to phase conversions. For S-waves, the reference frame of the observer facing the station with their back to the source is used, where a first-motion to the right is denoted by a positive polarity and a first-motion to the left is denoted by a negative polarity.

For the amplitude ratios, we follow the method of Havskov and Ottemoller (2010) and exclude amplitudes measured on the radial components as their associated free-surface corrections vary

rapidly with incidence angle. We therefore use the three amplitude ratios of  $\frac{SV_Z}{P_Z}$ ,  $\frac{SH_T}{P_Z}$  and  $\frac{SV_Z}{SH_T}$  only, where  $P_Z$ ,  $SV_Z$  and  $SH_T$  are the P-wave amplitudes on the vertical components, SV- on the vertical and SH- on the transverse respectively. Due to the relatively short traveltimes of the ARGOS events under consideration, the attenuation quality factors are small in comparison to the uncertainties in measuring the amplitudes and are ignored (Havskov and Ottemoller 2010). The free-surface corrections are assumed to be 1.7, 0.8 and 2.0 for the  $\frac{SV_Z}{P_Z}$ ,  $\frac{SH_T}{P_Z}$  and  $\frac{SV_Z}{SH_T}$  ratios respectively (Aki and Richards 2002). From the output list of possible solutions we select the mechanism with the least polarity errors and the lowest RMS error of the accepted amplitude ratios (see Table C.1). Uncertainties in dip and strike are also presented.

## 5. Results

### 5.1. Spatial Variation in Seismicity

Using the Aluto seismic network we locate 2142 earthquakes, of which 1361 are situated within 15 km of the centre of the caldera, which is defined as station A01E (Fig. 4). For these events within 15 km, we obtain median location uncertainties, defined as the one standard deviation standard confidence level of the PDF scatter cloud, of  $\pm 3.31$  km in longitude,  $\pm 3.17$  km in latitude and  $\pm 2.57$  km in depth, with 50.9% of the catalogue containing a maximum uncertainty  $< 4$  km (Fig. 4c). We note that the lower median uncertainties in depth compared to in longitude and latitude may be influenced by station topography, where for shallow events (the majority of the catalogue), raypaths propagate laterally and the uncertainty in depth is approximately equal to the horizontal uncertainty (e.g. for events below 5 km b.s.l. the median uncertainties are 2.96, 2.71 and 3.24 km in longitude, latitude and depth respectively).

A subset of 693 events with maximum uncertainties of 4 km is presented in Fig. 4. In this subset, abundant seismicity is evident at shallow depths with 369 events occurring between the surface and sea level of which, 202 events occur within the uppermost 500 m. There is a relatively aseismic region beneath this, with 39 earthquakes occurring between 0 and 2 km b.s.l. but a more seismically active region between 2 and 9 km b.s.l. containing 239 events. This seismogenic layer deepens down to  $\sim 15$  km with latitude, to both the north and south of the volcanic edifice. Little seismicity is detected below 9 km, where only 48 events occur.

There is an alignment of events along the AJFZ that trends parallel to the WFB at  $\sim N012^\circ E$  (Agostini et al. 2011). This provides a narrow peak centred at  $38.79^\circ E$  in the histogram of events with longitude, where 44.9% occur between  $38.77^\circ E$  and  $38.81^\circ E$ . The pattern of seismicity with latitude produces a weakly bimodal distribution, where fewer events occur beneath the caldera relative to the regions directly to the north and south of the caldera rim. Relatively few events are located on the border faults to the east of Aluto, although we note that this region is outside the aperture of the recording network. The overall spatial distribution of events is further supported through the double-differenced earthquake relocations (Waldhauser and Ellsworth 2000) presented in Appendix A.

### 5.2. Seismicity and Anthropogenic Activity

From Fig. 4b, we do not observe any consistent spatio-temporal patterns in seismicity beneath Aluto with the event distribution appearing scattered. Over the two years the average seismicity rate of events occurring within 15 km of the edifice was 1.81 earthquakes per day. During the experiment, the power plant was in operation from 14th January 2012 until 4th July 2012, a relatively small proportion of the recording span of the network. Unfortunately no data regarding fluid injection or extraction rates are available during this operational period and it is therefore difficult to comment on the plant's impact on local seismicity as a result. Nonetheless, we do not

observe any significant changes between periods of power generation and periods of elevated seismicity.

### 5.3. Magnitudes and b-Values

Local magnitudes for the Aluto event catalogue of 1361 earthquakes (Fig. 4) range from -0.39 to 2.98 (Fig. 5a). Due to their relatively small sizes, none of the Aluto events were recorded by the Institute of Geophysics, Space Science and Astronomy (IGSSA) based at Addis Ababa University. We calculate the seismic energy release for the 1361 located earthquakes around the caldera using empirical relationships for  $M_L$  (Kanamori 1977; Keir et al. 2011), which totals  $3.80 \times 10^{14}$  Nm over the span of the deployment ( $1.85 \times 10^{14}$  Nm/yr). This value and that of the total moment release from all 2142 ARGOS events ( $4.49 \times 10^{15}$  Nm/yr) are approximately 3–5 orders of magnitude less than the predicted moment released from geodetic modelling in the MER (Déprez et al. 2013) and agree with the dominant aseismic release of moment within the rift (Hofstetter and Beyth 2003). We do not observe any clear spatial relationships between  $M_L$  and event location (Fig. 4).

In tectonic settings, the b-value is generally close to 1 (Frohlich and Davis 1993) but anomalous values as high as 3 have been observed in volcanic areas where the accumulation of strain may be preferentially released by numerous relatively small events (e.g., Wiemer and McNutt 1997; Murru and Montuori 1999; Wyss et al. 2001). For these Aluto events we determine a b-value of  $1.40 \pm 0.14$  to the 95% confidence level and a magnitude of completeness ( $M_C$ ) equal to 1.35 (Fig. 5). We find that only considering a subset of the best located events (< 4 km uncertainty) into the calculation does not improve the uncertainties of the derived b-value.

We next calculate the b-value incrementally with depth (Fig. 6). Events are binned into overlapping horizontal slices of 2 km thickness at 0.5 km spacings down to 10 km, below which seismicity is too sparse to successfully fit the Gutenberg-Richter relationship within each bin. The a-value is also presented and reflects the relative seismicity rate. This depth mapping shows three regions of contrasting b in the uppermost 10 km (Fig. B.1):

- 2–0 km:** A b-value of  $2.55 \pm 0.55$  and high seismicity rate ( $a = 5.64$ ) where 796 events occur.
- 0–2 km:** A reduced b-value of  $0.82 \pm 0.21$  and a lower a-value of 2.49 where 90 events occur.
- 2–9 km:** Elevated b-values ranging from 0.95 to 1.33 and increased seismicity, where a-values are 2.69–3.53 and 111–145 events occur within each depth bin.

### 5.4. Focal Mechanisms

We compute source mechanisms for 21 earthquakes around Aluto (Figs. 7 and Appendix B), finding that incorporating SH-wave polarities and amplitude ratios helps to reduce ambiguity in the grid-searches. The focal mechanisms beneath Aluto are predominantly normal events with rakes less than  $-22.2^\circ$  and an average rake of  $-56.9^\circ$ . Generally, the events that we determine mechanisms for occur close to the AJFZ and to Quaternary to Recent faults associated with the WFB. Some events (e.g., 11, 14, 17, 18, 20 and 21) have left-lateral strike-slip components that occur on ~NE striking fault planes however.

The overall mean azimuth of the T-axes is N098°E, which is approximately perpendicular to the strike of the WFB and the average T-axes plunge is  $10.8^\circ$  (Fig. 8). The P-axes of the fault solutions cluster towards the centre of the hemispherical projections, with a mean azimuth of N276.0°E and an average plunge of  $62.0^\circ$ .

## 6. Discussion

### 6.1 Magmatic System

At depths below 9 km there is little seismicity, which agrees with the hypothesis that beneath this depth, rift extension in the MER is accommodated aseismically and associated with ductile stretching (Daniels et al. 2014) and/or magmatic injection into the lower to mid-crust (Ebinger and Casey 2001; Keir et al. 2006a). In the Boset-Kone volcanic segment to the north, earthquakes deeper than 10 km are also relatively sparse and are indicative of an elevated heat flow that inhibits brittle deformation (Maggi et al. 2000). This is suggestive of a hot, ductile magmatic mush zone as Aluto's primary magmatic reservoir where little seismicity occurs as a consequence (Fig. 9). We acknowledge however that with the uncertainty of the precise location of Aluto's magma reservoir (Samrock et al. 2015), that melt may be present at greater depths than this. This may consequently raise the brittle-ductile transition depth above it and produce relatively shallower earthquakes beneath the caldera than to the north and south.

Modelling of edifice-wide inflation occurring at Aluto in 2008 suggests a deformation source at 3.1 km depth and is interpreted to reflect the episodic intrusion of magma into a volatile-rich cap between the magmatic and hydrothermal reservoirs (Hutchison et al. 2016). Since deformation modelling is most sensitive to the top surfaces of inflating or deflating sources (Yun et al. 2006), this implies that magma ascent does not propagate shallower than this depth, and is broadly consistent with MT surveying, which has failed to image conductive magmatic phases above 5 km (Samrock et al. 2015).

Between 2 and 9 km b.s.l. we observe a region of increased seismicity and high b-values of up to 1.33. Elevated b-values associated with magmatic intrusion have been previously attributed to increases in pore pressures (reducing the effective stress) and the propagation of cracks (increasing heterogeneity) as magmas migrate (Mogi 1962; Wyss 1973). With intrusion interpreted to drive inflation episodes at the surface, we suggest that the seismicity distribution within this zone also reflects these volcanic processes. In this case, high strain rates and an elevated b-value are induced via magmatic injection from a larger magma reservoir below.

Furthermore, the mapping of b-values at Mt. St. Helens and Mt. Spurr (Wiemer and McNutt 1997) and at the Long Valley Caldera (Wiemer et al. 1998) has also shown that regions of high b-values correlate well with regions of gas vesiculation from ascending magmas. We speculate that towards the top of the magmatic system (2–3 km b.s.l.), that the exsolution of volatiles also contributes to the observed b-value anomaly, where violent vesiculation fractures the rock volume at the deformation source and microseismicity is induced around it.

## 6.2 Hydrothermal System

Above this region of volatile release and between 0 and 2 km, we detect a region of reduced seismicity where elastic deformation is diminished. The b-value also decreases to below unity, which implies an increase in friction and that seismicity is not fluid induced. Although CO<sub>2</sub> gas sampling of fumaroles has shown that the magmatic and hydrothermal systems are connected (Teklemariam et al. 1996; Hutchison et al. 2016), the sparse seismicity and relatively low b-value suggests that during 2012 and 2013 that this pathway was relatively impermeable.

The modelling of unrest at Campi Flegrei in Italy has suggested that deformation cycles begin with the injection of magmatic phases into an impermeable cap that exsolve volatiles as the magma crystallises (Battaglia et al. 2006). Vesiculated fluids have been shown to preferentially form in horizontal lenses, in which case permeability anisotropy may inhibit the volatiles' ascent into the hydrothermal system (Fournier 1999). A self-sealed zone of precipitates provides the impermeable barrier that then segregates the shallower hydrothermal field from the magmatic reservoir and causes surface uplift as volatiles accumulate beneath the barrier.

At some critical point the impermeable barrier is breached under the increasing pressure and volatiles ascend to the brittle, lower pressured aquifer through faulting and brecciation of the medium and induces seismicity. This increases the pore pressure and temperature within the shallow aquifer, with the efficient discharge of fluids via lateral flow facilitating subsequent subsidence (De Natale et al. 2001). A similar model of unrest has also been suggested at Aluto by Biggs et al. (2011) where inflation episodes are attributed to magmatic activity perturbing the hydrothermal system and subsidence episodes attributed to the hydrothermal system only.

The deformation source of subsidence at Aluto between 2009 and 2010 has been modelled as a Mogi point source at 1.4 km depth (Fig. 9), which like at Campi Flegrei, represents the loss of fluid from the hydrothermal system (Hutchison et al. 2016). Assuming the same source location for the 2012 subsidence places the source within the observed aseismic region but the faulting associated with the release of volatiles at the onset of subsidence is not observed in the seismicity distribution within this depth region. At Aluto, the continued subsidence observed from December 2009 (Biggs et al. 2011) suggests that it is likely that the faulting and volatile ascent associated with the onset of subsidence occurred before the deployment of the seismic network. The associated faulting had subdued by 2012, with the self-sealing of the volatile cap recommencing quickly as further volatiles accumulated. The relatively prolonged deflation suggests that lateral flow and hydrothermal processes continued to dominate the surface expression of the system however, and that despite the fast resealing of the impermeable layer, inflation was not observed again until mid-2013 (Hutchison et al. 2016).

Areas of enhanced thermal gradients, such as within geothermal regions are often related to rocks of weak rheologies where failure may ensue at relatively low shear stresses (Warren and Latham 1970; Wyss 1973). This can lead to b-values greater than 1 (Bachmann et al. 2012; Trugman et al. 2016). The overall b-value at Aluto of  $1.40 \pm 0.14$  indicates an elevated number of small magnitude events relative to larger ones and sits in agreement. This is particularly evident in the uppermost 2 km, where the b-value is  $2.55 \pm 0.55$  and is significantly greater than a value calculated for the wider MER region of  $1.13 \pm 0.05$  (Keir et al. 2006b). At Aluto it is likely that the highly fractured nature of the AJFZ, assumed ring faulting and high thermal-gradient driving the geothermal system (Hutchison et al. 2015a), all aid in promoting failure at low shear stresses that generates the highest seismicity rates and significantly elevates the b-value.

Well-log data has revealed that the geothermal reservoir resides in a Neogene ignimbrite unit at approximately sea level (Teklemariam et al. 1996) (Figs. 2 & 9). In the hottest wells at LA-4 and LA-6, temperatures in excess of  $340^{\circ}\text{C}$  have been recorded at 2100 m below the surface ( $\sim 150$  m b.s.l., Gizaw 1993), hence suggesting a temperature gradient of  $\sim 160\ ^{\circ}\text{C}/\text{km}$ . High b-values associated with the migration and circulation of hydrothermal fluids have also been presented at the Yellowstone caldera (Farrell et al. 2009), where a region of  $b = 1.3 \pm 0.1$  correlates well with hydrothermal features mapped at the surface. Although our derived value within the hydrothermal system is much greater than this value, the estimated temperature gradient at Aluto is up to twice that at Yellowstone ( $50\text{--}80\ ^{\circ}\text{C}/\text{km}$ ), suggesting a more energetic geothermal system that induces relatively more microseismic events.

Elevated b-values have also been presented at geothermal fields in California, where at the Geysers, Salton Sea and Coso, high values of over 1.3 using a moving window of 400 events have been correlated with geothermal power production at each field (Trugman et al. 2016). At Coso, a b-value as high as 2.4 has also been determined using a one-year moving window approach that incorporated 1000s of events into each calculation (Kaven et al. 2013). In addition, b-values of up to 3.5 were determined at the Basel EGS experiment during co- and post-injection stages (Bachmann et al. 2012), further highlighting the prevalence of short earthquake recurrence times in regions of low friction at geothermal sites.

The high fluid saturation and permeability of the shallow hydrothermal system region is likely amplified by its highly fractured nature with some contribution from the condensation of geothermal gases that ascend along the AJFZ (Gizaw 1993). The temporal distribution of shallow (<2 km) Aluto events in relation to the hydrostatic loading (precipitation) and elastic response of the surface (deformation inferred from GPS) has suggested that periods of high rainfall replenish the hydrothermal system, where a cross-correlation of shallow seismicity and rainfall suggests that peak seismicity follows peak rainfall after ~4 months (Birhanu et al. 2017.). This estimated lag time is broadly consistent with results seen elsewhere in the MER (Birhanu and Bendick 2015) and provides further evidence that fluid saturation of the subsurface and circulation in the geothermal reservoir plays an important role in the seismic response of the volcano.

### 6.3. Rift Structures

Since 2 Ma, strain in the MER has localised to right-stepping en-echelon rift segments that are largely controlled by the intrusion of mafic magmas as rifting has evolved towards continental break-up (Boccaletti et al. 1998; Ebinger and Casey 2001; Keir et al. 2015). This migration of strain localisation to the centre of the rift is commonplace during magma-assisted rifting (Buck 2004), where the decreasing strength of the lithosphere prevents the stress levels of boundary faults from reaching failure. The sparseness of seismicity on the border faults to the east of Aluto suggests that this is the case, while the alignment of seismicity along the AJFZ and WFB at ~N012°E, rather than along the border faults at ~N032° E, highlights that these are currently the active structures (Agostini et al. 2011).

The source mechanisms at Aluto are predominantly normal or normal with some small component of strike-slip. These events are in close agreement with mechanisms produced previously along a large proportion of the MER (e.g., Foster and Jackson 1998; Hofstetter and Beyth 2003; Keir et al. 2006a), where events have occurred on steeply-dipping normal faults striking approximately NNE. The average T-axis azimuth of these events of N098°E is perpendicular to the average strike of the WFB (Agostini et al. 2011) and suggests that the overall orientation of minimum compression at Aluto is congruent to that of present-day rifting at ~N100°E (Stamps et al. 2008).

Exceptions to this typical trend of normal dip-slip in the MER include strike-slip events on NE-ENE structures, where left-lateral offsets have been observed by Foster and Jackson (1998), Ayele (2000) and Keir et al. (2006a). This has been particularly evident at the tips of magmatic segments and is thought to represent transcurrent motion where deformation is additionally complex (Casey et al. 2006; Beutel et al. 2010). Beneath Fentale and Boset for example, left-lateral slip has been associated with displacement on pre-3.5 Ma structures that formed prior to the onset of magma-assisted rifting in the CMER at 2 Ma (Keir et al. 2006a). At Aluto, which is located at the southern tip of the Aluto-Gedemsa magmatic segment, we suggest that the components of strike-slip in certain events likely arises in this manner and may be indicative of the reactivation of such structures oblique to the direction of present-day extension.

## 7. Conclusions

Using a local network of 12 seismic stations, the seismicity at Aluto has been monitored for the first time. Prior to this, the volcano was known to be deforming but no seismicity had been detected with regional or national networks. We detect 2142 earthquakes around Aluto over a two year period, of which 1361 occur within 15 km of the volcanic edifice. Shallow events are interpreted in terms of hydrothermal activity in the uppermost 2 km, whilst the relatively sparser, deeper events are most likely associated with magmatic processes. Of the best located events, focal depths range from the near surface to a maximum of 15 km with a significant amount of seismicity following NNE-SSW faulting through the caldera and in alignment with the Quaternary to Recent

rifting of the WFB. Focal mechanisms are normal or normal with small components of strike-slip and show shallow dipping T-axes orientated parallel to current extension.

We utilise a local magnitude scale that provides event sizes beneath the volcanic centre ranging between  $-0.40$  and  $2.98$ . Resembling many volcanic and geothermal settings, we observe a high overall b-value of  $1.40 \pm 0.14$  that suggests that seismic moment release occurs through numerous relatively small events. This is particularly evident in the hydrothermal layer (above sea level), where b reaches  $2.55$  and the additional influence of high precipitation and subsequent gravitational loading likely contributes to the release of accumulated strain in numerous microseismic events.

The b-value varies with depth however, with low values and a relatively low seismicity rate between  $0$  and  $2$  km suggesting a comparatively stronger rheology and increased friction. The low seismicity within this layer likely indicates low permeability that suppresses the ascent of magmatic fluids to the hydrothermal system and implies that processes within the hydrothermal system are the primary control on surface deformation.

The b-value and seismicity rate increases between  $2$ – $9$  km, which suggests that high strain rates and the interaction of magmatic fluids promote elastic deformation, magmatic intrusion and gas vesiculation that in turn, drive short periods of uplift at the surface. Little seismicity occurs beneath these depths nor to the eastern border faults, supporting the theory that strain localised towards the centre of the rift at  $2$  Ma and was heavily associated with magmatic processes.

Aluto is an active volcano that has highlighted its seismogenic nature despite no volcanic eruptions for at least  $2000$  years. Local seismicity observations have been presented and along with previous and on-going geodetic observations and the areas' growing economic importance, we recommend further geophysical monitoring of Aluto and of other volcanoes within the MER.

## **8. Acknowledgements**

We would like to thank SEIS-UK for the use of their equipment, for their help whilst in the field and upon managing the data when back in the UK. Likewise, we thank various collaborators from the Ethiopian Electric Power Corporation (EEPCo) and the Geological Survey of Ethiopia (GSE) for their contributions to the project. The Bristol University Microseismic ProjectS (BUMPS) provided funding for the seismic experiment and fieldwork and the seismic equipment was loaned from SEIS-UK with GEF loan 962. The seismic network is XM and the dataset is open access and available on IRIS. M.W. was funded by an EPSRC studentship. The research leading to these results has received funding from the European Research Council under the European Union's Seventh Framework Programme (FP7/2007-2013)/ERC grant agreement 240473 "CoMITAC". A.N. was funded by BUMPS and CoMITAC and J.B. was funded by NERC COMET.

## **9. Appendices**

### **9.A. Double-Difference Earthquake Locations**

To negate the effects of a poorly constrained velocity model causing inaccuracies in the event locations, it is common practise to refine hypocentre locations using the double-differencing technique described by Waldhauser & Ellsworth (2000). This technique can revise initial event locations to highlight the clustering of earthquakes and better resolve subsurface features in cases where the hypocentral separation between an earthquake pair is small, in comparison to the source-station distance. In this scenario, it is assumed that the raypaths between the events and the common station are similar and that the difference in traveltimes is due to spatial offset between the events.

First, catalogue phase data (output from *NONLINLOC*) is pre-processed to derive traveltimes differences between earthquake pairs. A ‘network of links’ is created by examining every event and comparing it spatially to other proximal events within some maximum radius. The maximum radius should however be small in comparison to the source-station distance and the length of the subsurface velocity heterogeneity but similar to the uncertainties of the initial locations.

‘Neighbouring’ events are then determined using a nearest neighbour approach. Through solving the double-differencing equations with the computed differential traveltimes as outlined by Waldhauser & Ellsworth (2000), clusters within the initial catalogue are then relocated.

We follow this approach at Aluto using the 1D velocity model described in Table 1. Clustering the 693 best-located events (uncertainties <4km) from the Aluto catalogue by grouping events into bins of 1 km radius relocates 218 events in 79 clusters (Fig. A.1). With a high proportion of the Aluto catalogue by nature, occurring close to the volcanic centre and at relatively shallow depths, not all earthquake pairs have a hypocentral separation significantly less than the source to station distance. This is reflected by the relatively low number (31%) of earthquakes that are relocated when using this technique.

The relocations cluster along the AJFZ and highlights that seismicity trends NNE- SSW in agreement with the locations from *NONLINLOC*. A sharp peak at  $38.79^{\circ}$ - $38.80^{\circ}$  is observed that emphasises this further. Few events are relocated directly beneath the caldera in comparison to regions to the north and south of the rim, creating a bimodal distribution with latitude.

### 9.B. b-Values with Depth

Estimating b-values for four depth ranges for the 1361 earthquakes around Aluto shows three regions of contrasting  $b$  (Fig. B.1). Between the surface and sea level and where seismicity is highest, we calculate a b-value of 2.55, which even with relatively large uncertainties of  $\pm 0.55$  suggests a b-value well above 1 that is indicative of swarm activity. In the relatively aseismic region between 0 and 2 km,  $b$  is reduced to  $0.82 \pm 0.21$  and is more aligned to the global tectonic average. Below 2 km, the two regions above and below 9 km produce b-values of  $1.25 \pm 0.28$  and  $1.20 \pm 0.34$  that are again suggestive that strain is preferentially released via numerous relatively small magnitude events, relative to tectonic settings.

### 9.C. Focal Mechanisms

The parameters output from *FOCMEC* for the 21 focal mechanisms are presented in Fig. C.1 and Table C.1. The best fitting fault plane solutions for each event are presented with the fractions of P- and SH-wave polarities that correctly fit the output quadrants. For the amplitude ratios, the fraction denotes the number of acceptable ratios divided by the total number of ratios input into the grid-search, while the RMS error is the RMS of the accepted ratio observation

## 10. References

Agostini, A., Bonini, M., Corti, G., Sani, F., Mazzarini, F., 2011. Fault architecture in the Main Ethiopian Rift and comparison with experimental models: Implications for rift evolution and Nubia-Somalia kinematics. *Earth and Planetary Science Letters* 301 (3-4), 479–492.

Aki, K., 1965. Maximum Likelihood Estimate of  $b$  in the Formula  $\log N = a - bM$  and its Confidence Limits. In: University of Tokyo Earthquake Research Institute Bulletin. Vol. 43. Earthquake Research Institute of the University of Tokyo, Tokyo, Japan., pp. 237–239.

Aki, K., Richards, P. G., 2002. Quantitative Seismology, 2nd Edition. University Science Books, Sausalito, California.

Ayele, A., 2000. Normal left-oblique fault mechanisms as an indication of sinistral deformation between the Nubia and Somalia Plates in the Main Ethiopian Rift. *Journal of African Earth Sciences* 31 (2), 359–367.

Ayele, A., Stuart, G. W., Bastow, I. D., Keir, D., 2007. The August 2002 earthquake sequence in north Afar: Insights into the neotectonics of the Danakil microplate. *Journal of African Earth Sciences* 48 (2-3), 70–79.

Bachmann, C. E., Wiemer, S., Goertz-Allmann, B. P., Woessner, J., 2012. Influence of pore-pressure on the event-size distribution of induced earthquakes. *Geophysical Research Letters* 39 (9), L09302.

Battaglia, M., Troise, C., Obrizzo, F., Pingue, F., De Natale, G., 2006. Evidence for fluid migration as the source of deformation at Campi Flegrei caldera (Italy). *Geophysical Research Letters* 33, L01307.

Belachew, M., Ebinger, C. J., Cote, D., 2012. Source mechanisms of dike-induced earthquakes in the Dabbahu-Manda Hararo rift segment in Afar, Ethiopia: implications for faulting above dikes. *Geophysical Journal International* 192 (3), 907-917.

Beutel, E., van Wijk, J., Ebinger, C., Keir, D., Agostini, A., 2010. Formation and stability of magmatic segments in the Main Ethiopian and Afar rifts. *Earth Planetary Science Letters* 293, 225–235.

Biggs, J., Bastow, I. D., Keir, D., Lewi, E., 2011. Pulses of deformation reveal frequently recurring shallow magmatic activity beneath the Main Ethiopian Rift. *Geochemistry, Geophysics, Geosystems* 12 (9), 1-11.

Birhanu, Y., Bendick, R., 2015. Monsoonal loading in Ethiopia and Eritrea from vertical GPS displacement time series. *Journal of Geophysical Research: Solid Earth* 120 (10), 7231–7238.

Birhanu, Y., Wilks, M., Biggs, J., Lewi, E., Kendall, J.- M., Ayele, A., Bekele, B., 2017. The response to precipitation of a hydrothermal system: seasonal seismicity and vertical deformation at Aluto – Langano, Ethiopia. (In submission)

Boccaletti, M., Bonini, M., Mazzuoli, R., Abebe, B., Piccardi, L., Tortorici, L., 1998. Quaternary oblique extensional tectonics in the Ethiopian Rift (Horn of Africa). *Tectonophysics* 287 (1-4), 97–116.

Bonini, M., Corti, G., Innocenti, F., Manetti, P., Mazzarini, F., Abebe, T., Pecskay, Z., 2005. Evolution of the Main Ethiopian Rift in the frame of Afar and Kenya rifts propagation. *Tectonics* 24, TC1007.

Buck, W. R., 2004. Consequences of asthenospheric variability on continental rifting. In: Karner, G. D., Taylor, B., Driscoll, N. W., Kohlstedt, D. L. (Eds.), *Rheology and deformation of the lithosphere at continental margins*. Columbia University Press, Ch. 1, pp. 1–30.

Casey, M., Ebinger, C. J., Keir, D., Gloaguen, R., Mohamed, F., 2006. Strain accommodation in transitional rifts: extension by magma intrusion and faulting in Ethiopian rift magmatic segments. In: Yirgu, G., Ebinger, C. J., Maguire, P. K. H. (Eds.), *The Afar Volcanic Province within the East African Rift System*. Vol. 259. Geological Society of London, London, Special Publications, Ch. 3, pp. 143–163.

Chorowicz, J., 2005. The East African rift system. *Journal of African Earth Sciences* 43 (1-3), 379–410.

Christensen, N. I., 1984. Seismic Velocities. In: Carmichael, R. S. (Ed.), *Handbook of physical properties of rocks*, Vol. 2. CRC Press, Boca Raton, Florida, p. 228.

Cornwell, D. G., Mackenzie, G. D., England, R., Maguire, P. K. H., Asfaw, L., Oluma, B., 2006. Northern Main Ethiopian Rift crustal structure from new high-precision gravity data. In: Yirgu, G., Ebinger, C. J., Maguire, P. K. H. (Eds.), *The Afar Volcanic Province within the East African Rift System*. Vol. 259. Geological Society of London, London, Special Publications, Ch. 4, pp. 307–321.

Dakin, F. M., Gibson, I. L., 1974. A preliminary account of Alutu, a pantelleritic volcano in the Main Ethiopian Rift. *Bulletin of the Geophysical Observatory*, Haile Selassie I University, Addis Ababa 13, 110–114.

Daly, E., Keir, D., Ebinger, C. J., Stuart, G. W., Bastow, I. D., Ayele, A., 2008. Crustal tomographic imaging of a transitional continental rift: the Ethiopian rift. *Geophysical Journal International* 172 (3), 1033–1048.

Daniels, K. A., Bastow, I. D., Keir, D., Sparks, R. S. J., Menand, T., 2014. Thermal models of dyke intrusion during development of continent-ocean transition. *Earth and Planetary Science Letters* 385, 145–153.

Darling, W. G., Gizaw, B., Arusei, M. K., 1996. Lake-groundwater relationships and fluid-rock interaction in the East African Rift Valley: isotopic evidence. *Journal of African Earth Sciences* 22 (4), 423–431.

De Natale, G., Troise, C., Pingue, F., 2001. A mechanical fluid-dynamical model for ground movements at Campi Flegrei caldera. *Journal of Geodynamics* 32 (4-5), 487–517.

Déprez, A., Doubre, C., Masson, F., Ulrich, P., 2013. Seismic and aseismic deformation along the east african rift system from a reanalysis of the GPS velocity field of Africa. *Geophysical Journal International* 193(3), 1353–1369.

Ebinger, C. J., Casey, M., 2001. Continental breakup in magmatic provinces: An Ethiopian example. *Geology* 29 (6), 527.

Ebinger, C. and Scholz, C.A., 2012. Continental rift basins: the East African perspective. *Tectonics of Sedimentary Basins: Recent Advances*, pp.183-208.

ELC Electroconsult, 1986. Exploitation of Langano-Aluto geothermal resources feasibility report. Tech. Rep., Ministry of Mines and Energy, Milano, Italy.

Farrell, J., Husen, S., Smith, R. B., 2009. Earthquake swarm and b-value characterization of the Yellowstone volcano-tectonic system. *Journal of Volcanology and Geothermal Research* 188 (1-3), 260–276.

Foster, A. N., Jackson, J. A., 1998. Source parameters of large African earthquakes: implications for crustal rheology and regional kinematics. *Geophysical Journal International* 134 (2), 422–448.

Fournier, R. O., 1999. Hydrothermal processes related to movement of fluid from plastic into brittle rock in the magmatic-epithermal environment. *Economic Geology* 94 (8), 1193–1211.

- Frohlich, C., Davis, S. D., 1993. Teleseismic b values; Or, much ado about 1.0. *Journal of Geophysical Research* 98 (B1), 631.
- Gianelli, G., Teklemariam, M., 1993. Water-rock interaction processes in the Aluto-Langano geothermal field (Ethiopia). *Journal of Volcanology and Geothermal Research* 56, 429–445.
- Gizaw, B., 1993. Aluto-Langano geothermal field, Ethiopian Rift Valley: Physical characteristics and the effects of gas on well performance. *Geothermics* 22 (2), 101–116.
- Goldstein, P., Snoke, J. A., 2005. SAC Availability for the IRIS Community. *Data Management Center Electronic Newsletter* 8 (1), 63.
- Gouin, P., 1979. Earthquake History of Ethiopia and the Horn of Africa. International Development Research Centre, Ottawa, Ontario.
- Grünthal, G., Bosse, C., Sellami, S., Mayer-Rosa, D., Giardini, D., 1999. Compilation of the GSHAP regional seismic hazard for Europe, Africa and the Middle East. *Annali di Geofisica* 42 (6), 1215–1223.
- Gutenberg, B., Richter, C. F., 1942. Earthquake magnitude, intensity, energy, and acceleration. *Bulletin of the Seismological Society of America* 32 (3), 163–191.
- Havskov, J., Ottemoller, L., 2010. *Routine Data Processing in Earthquake Seismology*. Springer, London, UK.
- Helffrich, G., Wookey, J., Bastow, I. D., 2013. *The Seismic Analysis Code, A Primer and User's Guide*. Cambridge University Press, Cambridge, UK.
- Hill, D. P., Bailey, R. A., Ryall, A. S., 1985. Active tectonic and magmatic processes beneath Long Valley Caldera, eastern California: An overview. *Journal of Geophysical Research* 90 (B13), 11111–11120.
- Hofstetter, R., Beyth, M., 2003. The Afar Depression: interpretation of the 1960-2000 earthquakes. *Geophysical Journal International* 155, 715–732.
- Hooper, A., Zebker, H., Segall, P., Kampes, B., 2004. A new method for measuring deformation on volcanoes and other natural terrains using InSAR persistent scatterers. *Geophysical Research Letters* 31, L23611.
- Hutchison, W., 2015. Past, present and future volcanic activity at restless calderas in the Main Ethiopian Rift. Doctor of philosophy, University of Oxford.
- Hutchison, W., Biggs, J., Mather, T. A., Pyle, D. M., Lewi, E., Yirgu, G., Caliro, S., Chiodini, G., Clor, L., Fischer, T., 2016. Causes of unrest at silicic calderas in the East African Rift: new constraints from InSAR and soil-gas chemistry at Aluto volcano, Ethiopia. *Geochemistry, Geophysics, Geosystems* 17 (8) 3008–3030.
- Hutchison, W., Mather, T. A., Pyle, D. M., Biggs, J., Yirgu, G., 2015a. Structural controls on fluid pathways in an active rift system: A case study of the Aluto volcanic complex. *Geosphere* 11 (3), 542–562.

Hutchison, W., Pyle, D. M., Mather, T. A., Yirgu, G., Biggs, J., Cohen, B. E., Barfod, D., Lewi, E., 2015b. The eruptive history and magmatic evolution of Aluto volcano: new insights into silicic peralkaline volcanism in the Ethiopian rift. *Journal of Volcanology and Geothermal Research*, 1–82.

International Seismological Centre, 2016. On-line Bulletin. Internat'l. Seis. Cent., Thatcham, United Kingdom. URL <http://www.isc.ac.uk>

Kagan, Y. Y., 1995. Magnitude-frequency distribution in the European-Mediterranean earthquake regions - Comment. *Tectonophysics* 245, 101–105.

Kanamori, H., 1977. The Energy Release in Great Earthquakes. *Journal of Geophysical Research* 82 (20), 2981–2987.

Kaven, J. O., Hickman, S. H., Davatzes, N. C., 2013. Micro-seismicity within the Coso Geothermal Field, California, from 1996–2012. In: Thirty-Eighth Workshop on Geothermal Reservoir Engineering. Vol. SGP-TR-198. Stanford University, Stanford, California, p. 10.

Kebede, S., Mamo, T., Abebe, T., 1985. Explanation to the Geological Map of Aluto-Langano Geothermal Area. Tech. rep., Ethiopian Institute of Geological Surveys, Addis Ababa, Ethiopia.

Keir, D., Bastow, I. D., Corti, G., Mazzarini, F., Rooney, T. O., 2015. The origin of along-rift variations in faulting and magmatism in the Ethiopian Rift. *Tectonics* 34, 464–477.

Keir, D., Ebinger, C. J., Stuart, G. W., Daly, E., Ayele, A., 2006a. Strain accommodation by magmatism and faulting as rifting proceeds to breakup: Seismicity of the northern Ethiopian rift. *Journal of Geophysical Research* 111 (B5), B05314.

Keir, D., Pagli, C., Bastow, I. D., Ayele, A., 2011. The magma-assisted removal of Arabia in Afar: Evidence from dike injection in the Ethiopian rift captured using InSAR and seismicity. *Tectonics* 30, TC2008.

Keir, D., Stuart, G. W., Jackson, A., Ayele, A., 2006b. Local Earthquake Magnitude Scale and Seismicity Rate for the Ethiopian Rift. *Bulletin of the Seismological Society of America* 96 (6), 2221–2230.

Laury, R. L., Albritton, C. C., 1975. Geology of Middle Stone Age Archaeological Sites in the Main Ethiopian Rift Valley. *Geological Society of America* 86 (7), 999–1011.

Le Turdu, C., Tiercelin, J. J., Gibert, E., Travi, Y., Lezzar, K. E., Richert, J. P., Massault, M., Gasse, F., Bonnefille, R., Decobert, M., Gensous, B., Jeudy, V., Tamrat, E., Mohammed, M. U., Martens, K., Atnafu, B., Chernet, T., Williamson, D., Taieb, M., 1999. The Ziway-Shala lake basin system, Main Ethiopian Rift: Influence of volcanism, tectonics, and climatic forcing on basin formation and sedimentation. *Palaeogeography, Palaeoclimatology, Palaeoecology* 150, 135–177.

Lomax, A., 2005. A Reanalysis of the Hypocentral Location and Related Observations for the Great 1906 California Earthquake. *Bulletin of the Seismological Society of America* 95 (3), 861–877.

Lomax, A., Curtis, A., 2001. Fast, probabilistic earthquake location in 3D models using oct-tree importance sampling. In: *Geophys. Res. Abstr. Vol. 3*. European Geophysical Society, Nice, France, p. 955.

Lomax, A., Virieux, J., Volant, P., Berge-Thierry, C., 2000. Probabilistic earthquake location in 3D and layered models - Introduction of a Metropolis-Gibbs method and comparison with linear

locations. In: Thurber, C. H., Rabinowitz, N. (Eds.), *Advances in Seismic Event Location*. Kluwer, Amsterdam, pp. 101–134.

Maggi, A., Jackson, J. A., McKenzie, D., Priestley, K., 2000. Earthquake focal depths, effective elastic thickness, and the strength of the continental lithosphere. *Geology* 28 (6), 495.

Maguire, P. K. H., Keller, G. R., Klemperer, S. L., Mackenzie, G. D., Keranen, K., Harder, S., O'Reilly, B., Thybo, H., Asfaw, L., Khan, M., Amha, M., 2006. Crustal structure of the northern Main Ethiopian Rift from the EAGLE controlled-source survey; a snapshot of incipient lithospheric break-up. Geological Society, London, Special Publications 259 (1), 269–292.

Midzi, V., Hlatywayo, D., Chapola, L., Kebede, F., Atakan, K., Lombe, D., Turyomurugyendo, G., Tugume, F., 1999. Seismic hazard assessment in Eastern and Southern Africa. *Annali di Geofisica* V42 (6), 1067–1083.

Mogi, K., 1962. Magnitude-Frequency Relation for Elastic Shocks Accompanying Fractures of Various Materials and Some Related Problems in Earthquakes. *Bulletin of the Earthquake Research Institute at the University of Tokyo* 40, 831–853.

Mohr, P. A., 1962. The Ethiopian Rift System. *Bulletin of the Geophysical Observatory of Addis Ababa* 5, 33–62.

Mohr, P. A., Mitchell, J. G., Raynolds, R. G. H., 1980. Quaternary volcanism and faulting at O'A caldera, Central Ethiopian Rift. *Bulletin Volcanologique* 43 (1), 173–189.

Moore, J. N., Allis, R. G., Nemcok, M., Powell, T. S., Bruton, C. J., Wannamaker, P. E., Raharjo, I. B., Norman, D. I., 2008. The evolution of volcano-hosted geothermal systems based on deep wells from Karaha-Telaga Bodas, Indonesia. *American Journal of Science* 308, 1–48.

Murru, M., Montuori, C., 1999. The Locations of Magma Chambers at Mt. Etna, Italy, mapped by b-values. *Geophysical Research Letters* 26 (16), 2553–2556.

Pizzi, A., Coltorti, M., Abebe, B., Disperati, L., Sacchi, G., Salvini, R., 2006. The Wonji fault belt (Main Ethiopian Rift): structural and geomorphological constraints and GPS monitoring. In: Yirgu, G., Ebinger, C. J., Maguire, P. K. H. (Eds.), *The Afar Volcanic Province within the East African Rift System*. Vol. 259. Geological Society of London, London, Special Publications, Ch. 3, pp. 191–207.

Podvin, P., Lecomte, I., 1991. Finite difference computation of traveltimes in very contrasted velocity models: a massively parallel approach and its associated tools. *Geophysical Journal International* 105 (1), 271–284.

Press, F., 1966. Seismic Velocities. In: Clark Jr., S. P. (Ed.), *Handbook of physical constants*. Vol. 97. Geological Society of America, New York, New York, Ch. 9, pp. 195–218.

Samrock, F., Kuvshinov, A., Bakker, J., Jackson, A., Fisseha, S., 2015. 3-D analysis and interpretation of magnetotelluric data from the Aluto-Langano geothermal field, Ethiopia. *Geophysical Journal International* 202 (3), 1923–1948.

Savage, M. K., Anderson, J. G., 1995. A local-magnitude scale for the western Great Basin-eastern Sierra Nevada from synthetic Wood-Anderson seismograms. *Bulletin of the Seismological Society of America* 85 (4), 1236–1243.

Siebert, L., Simkin, T., 2003. Volcanoes of the World: an Illustrated Catalog of Holocene Volcanoes and their Eruptions.

Snoke, J. A., 2003. FOCMEC: FOCal MEchanism determinations. In: Lee, W. H. K., Kanamori, H., Jennings, P. C., Kisslinger, C. (Eds.), International Handbook of Earthquake and Engineering Seismology. Vol. 85. Academic Press, San Diego, Ch. 12, pp. 1629–1630.

Snoke, J. A., Munsey, J. W., Teague, A. C., Bollinger, G. A., 1984. A program for focal mechanism determination by combined use of polarity and SV-P amplitude ratio data. *Earthquake Notes* 55, 15.

Sparks, R., S., J., Biggs, J., Neuberg., J., W., 2012. Monitoring Volcanoes. *Science* 335 (6074), 1310-1311.

Stamps, D. S., Calais, E., Saria, E., Hartnady, C., Nocquet, J.-M., Ebinger, C. J., Fernandes, R. M., 2008. A kinematic model for the East African Rift. *Geophysical Research Letters* 35, L05304.

Tarantola, A., 2005. Inverse Problem Theory and Methods for Model Parameter Estimation. Society for Industrial and Applied Mathematics, Philadelphia, PA.

Tarantola, A., Valette, B., 1982. Inverse problems = Quest for Information. *Journal of Geophysics* 50, 159–170.

Teklemariam, M., Battaglia, S., Gianelli, G., Ruggieri, G., 1996. Hydrothermal alteration in the Aluto-Langano geothermal field, Ethiopia. *Geothermics* 25 (6), 679–702.

Teklemariam, M., Beyene, K., 2002. Geochemical Monitoring of the Aluto-Langano Geothermal Field, Ethiopia. Tech. rep., Hydrogeology, Engineering Geology and Geothermal Department, Geological Survey of Ethiopia, Addis Ababa, Ethiopia.

Trugman, D. T., Shearer, P. M., Borsa, A. A., Fialko, Y., 2016. A comparison of long-term changes in seismicity at The Geysers, Salton Sea, and Coso geothermal fields. *Journal of Geophysical Research: Solid Earth* 121 (1), 225–247.

Utsu, T., 1965. A method for determining the value of b in a formula  $\log n = a - bM$  showing the magnitude-frequency relation for earthquakes. *Geophys. Bull. Hokkaido Univ* 13 (99), 103.

Waldhauser, F. & Ellsworth, W., 2000. A Double-Difference Earthquake Location Algorithm: Method and Application to the Northern Hayward Fault, California, *Bulletin of the Seismological Society of America*, 90(6), 1353–1368.

Warren, N. W., Latham, G. V., 1970. An experimental study of thermally induced microfracturing and its relation to volcanic seismicity. *Journal of Geophysical Research* 75 (23), 4455–4464.

Wiemer, S., McNutt, S. R., 1997. Variations in the frequency-magnitude distribution with depth in two volcanic areas: Mount St. Helens, Washington, and Mt. Spurr, Alaska. *Geophysical Research Letters* 24 (2), 189–192.

Wiemer, S., McNutt, S. R., Wyss, M., 1998. Temporal and three-dimensional spatial analyses of the frequency-magnitude distribution near Long Valley Caldera, California. *Geophysical Journal International* 134, 409–421.

Wilks, M., Ayele, A., Kendall, J.- M., Wookey, J., 2017. The 24<sup>th</sup> January 2016 Hawassa earthquake: Implications for seismic hazard in the Main Ethiopian Rift. *Journal of African Earth Sciences* 125, 118–125.

WoldeGabriel, G., Aronson, J. L., Walter, R., 1990. Geology, geochronology, and rift basin development in the central sector of the Main Ethiopia Rift. *Geological Society of America Bulletin* 102 (4), 439–458.

Wyss, M., 1973. Towards a Physical Understanding of the Earthquake Frequency Distribution. *Geophysical Journal International* 31 (4), 341–359.

Wyss, M., Klein, F., Nagamine, K., Wiemer, S., 2001. Anomalously high b-values in the South Flank of Kilauea volcano, Hawaii: evidence for the distribution of magma below Kilauea's East rift zone. *Journal of Volcanology and Geothermal Research* 106, 23–37.

Yang, Z. and Chen, W.P., 2008. Mozambique earthquake sequence of 2006: High-angle normal faulting in southern Africa. *Journal of Geophysical Research: Solid Earth*, 113(B12).

Yun, S., Segall, P., Zebker, H., 2006. Constraints on magma chamber geometry at Sierra Negra Volcano, Galapagos Islands, based on InSAR observations. *Journal of Volcanology and Geothermal Research* 150 (1-3), 232–243.

## **11. Figure Captions**

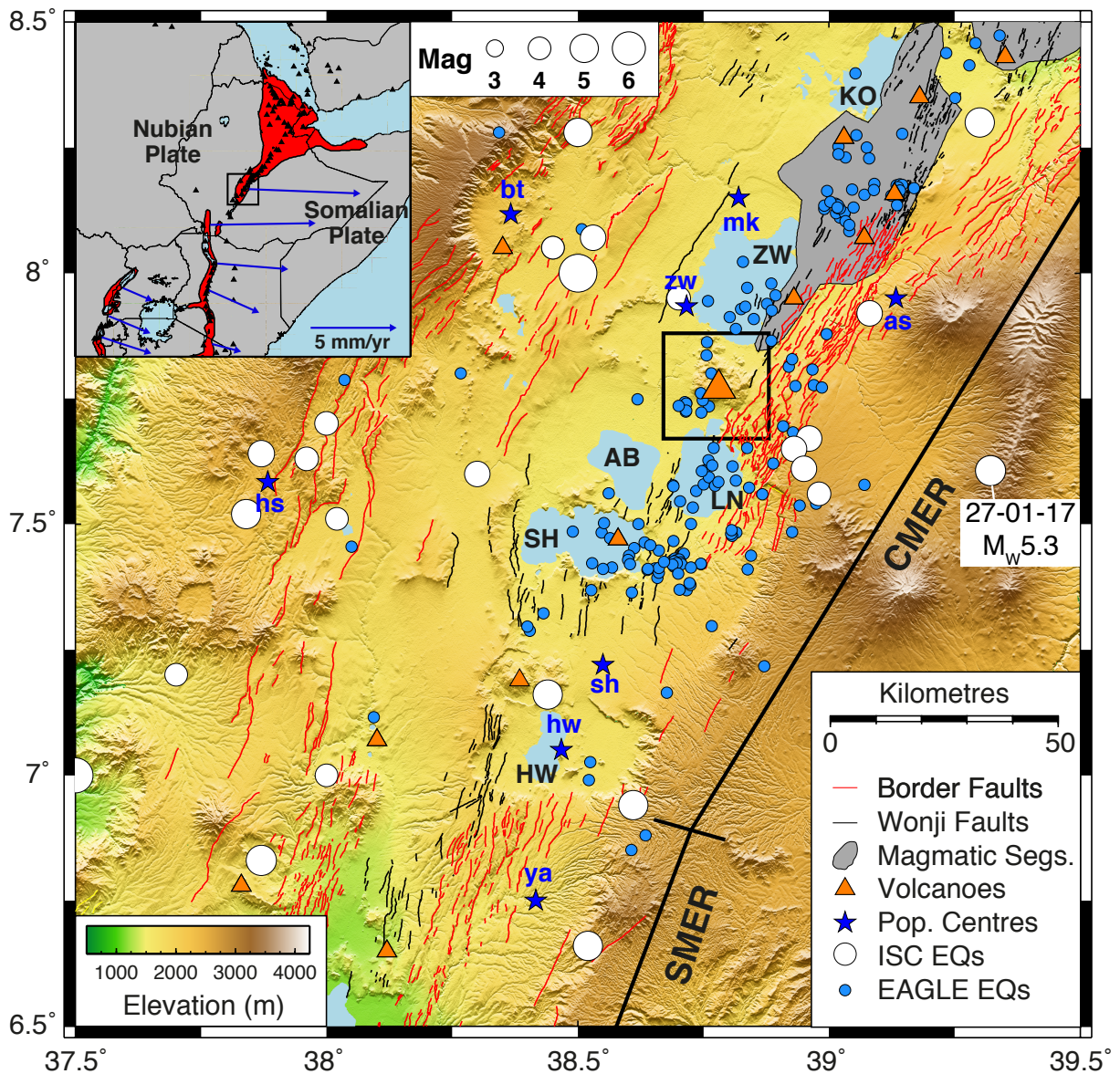


**Figure 1:** SRTM (<http://www2.jpl.nasa.gov/srtm>) elevation map of the Main Ethiopian Rift. Border faults of the rift's margins and internal faults of the Wonji Fault Belt (Agostini et al. 2011) are red and black lines respectively. Magmatic segments (Ebinger and Casey 2001) are grey and volcanoes active in the Holocene are orange triangles with Aluto enlarged (Siebert and Simkin 2003). Population centres of greater than 20,000 people (2007) are blue stars and labelled: mk: Meki; bt: Butajira; zw: Ziway; as: Assela; hs: Hosaena; sh: Shashemene; hw: Hawassa and ya: Yirga Alem. MER lakes are: KO: Lake Koka; ZW: Lake Ziway; LN: Lake Langano; AB: Lake Abijta; SH: Lake Shala and HW: Lake Hawassa. ISC reviewed earthquakes since 1960 (International Seismological Centre 2016) and seismicity recorded by the EAGLE project from October 2001 to January 2003 (Keir et al. 2006a) are white and blue circles with the MW5.3. Upper Left Inset: The study area's context within the East African Rift. Volcanoes are black triangles and vectors are the current day plate motions, scaled to extensional velocity and relative to the Nubian Plate (Stamps et al. 2008).

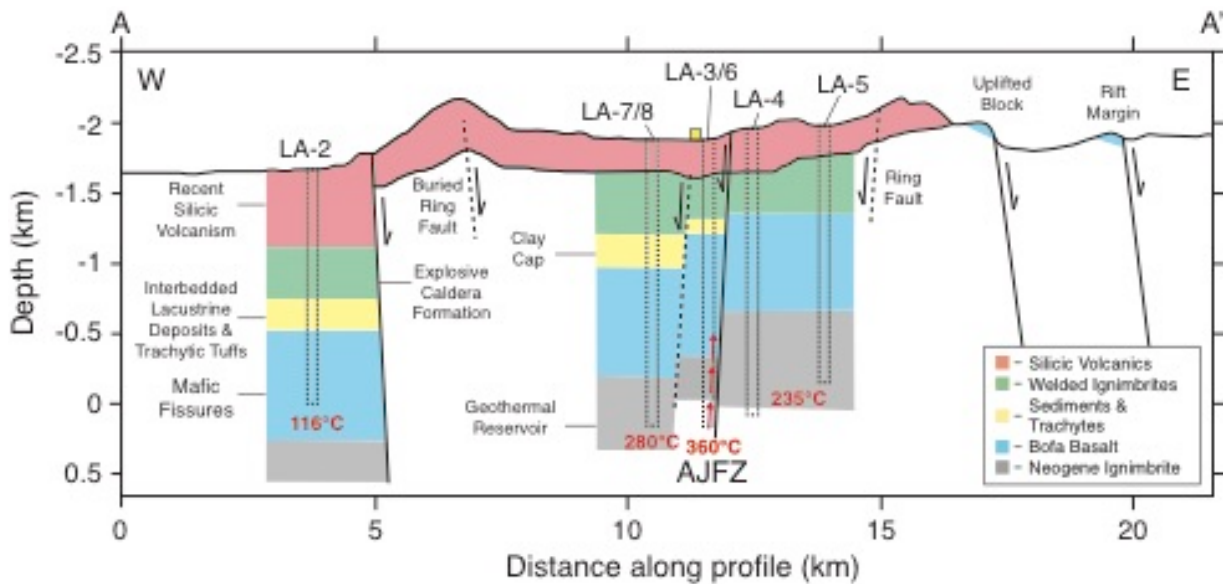


**Figure 2:** A cross-sectional summary of the stratigraphy beneath Aluto of the transect A-A' in Fig. 3 (after Hutchison et al. 2015a). Geothermal wells are projected onto the cross-section and labelled with temperatures recorded by Gizaw (1993). The Aluto- Langano Geothermal Plant is the yellow square. Faults and inferred faults are solid and dashed lines respectively with arrows denoting the up-flow of geothermal fluids along the AJFZ.

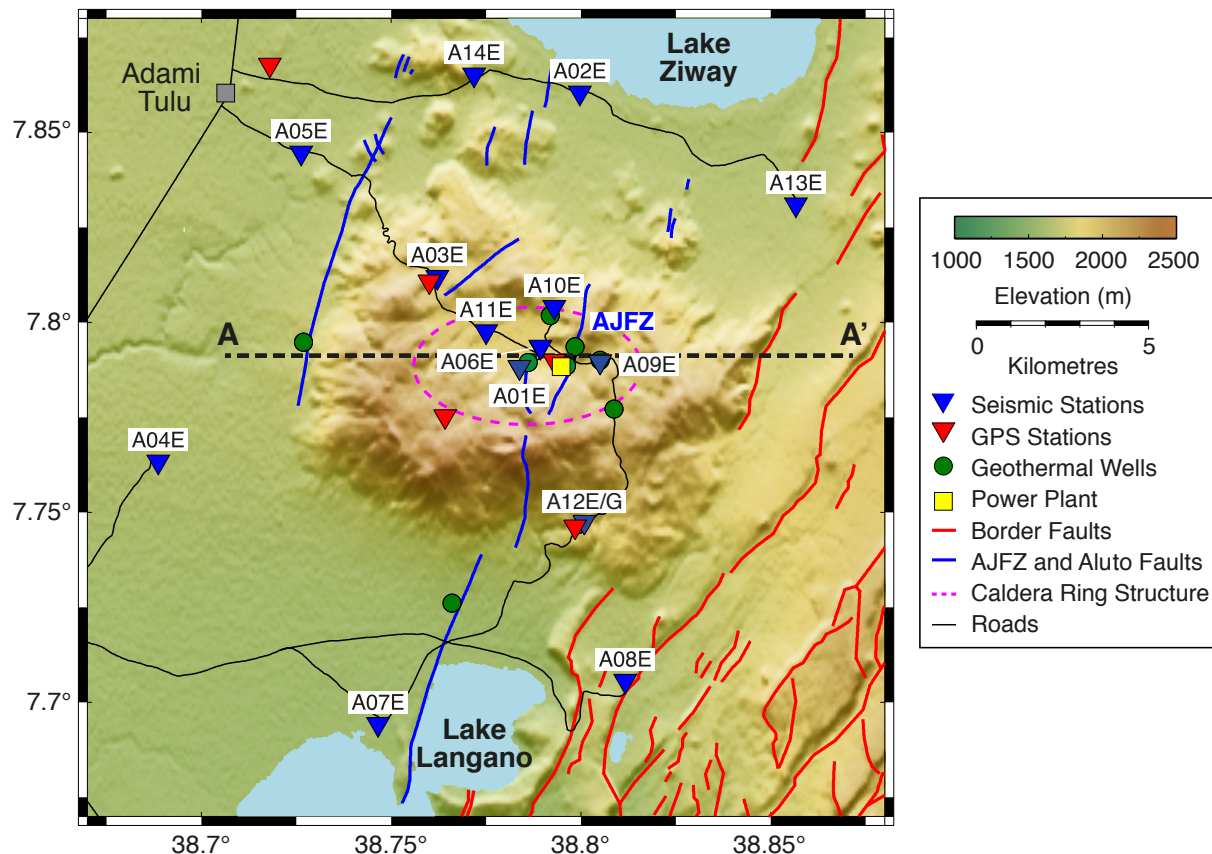


**Figure 3:** Topographic map of Aluto volcano. The stations of the ARGOS seismic network and GPS stations, the Aluto-Langano Geothermal Power Plant and geothermal wells. Border faults are red (Agostini et al. 2011) while the Artu Jawa fault zone (AJFZ) and other faults of the Aluto volcanic complex are blue (Kebede et al. 1985; Hutchison et al. 2015a). The caldera ring structure is the magenta dashed line (Hutchison et al., 2015a). The transect A-A' in Fig. 2 is the dashed back line.

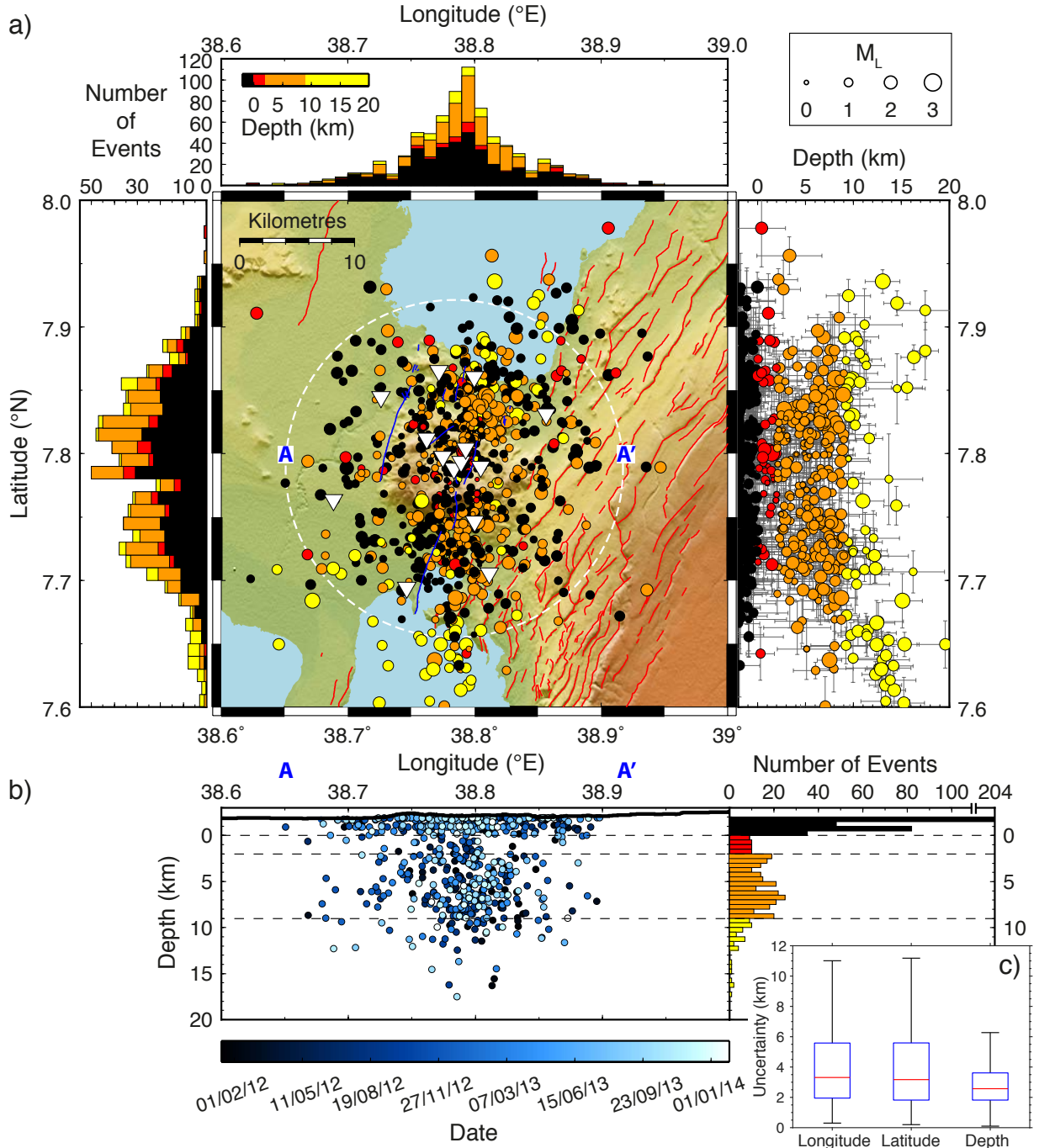


**Figure 4:** (a) The seismicity around Aluto with maximum location uncertainties <4 km plotted in map view and in a N-S depth profile with the associated errors bars. Events are coloured by four depth regions and sized by local magnitude. Zero depth is sea level. The 15 km radius from station A01E is the white dashed line. Seismic stations are inverted white triangles, border faults are red and the faults of the AJFZ and the Aluto volcanic complex are blue. Stacked histograms in longitude and latitude use bins of  $0.01^\circ$  width and are coloured by depth. (b) 693 earthquake hypocentres of events within 15 km of A01E along transect A-A'. Events are coloured by origin date. The histogram plots event depths in 0.5 km bins. (c) Box plots of the estimated location uncertainties in longitude, latitude and depth for all located events.

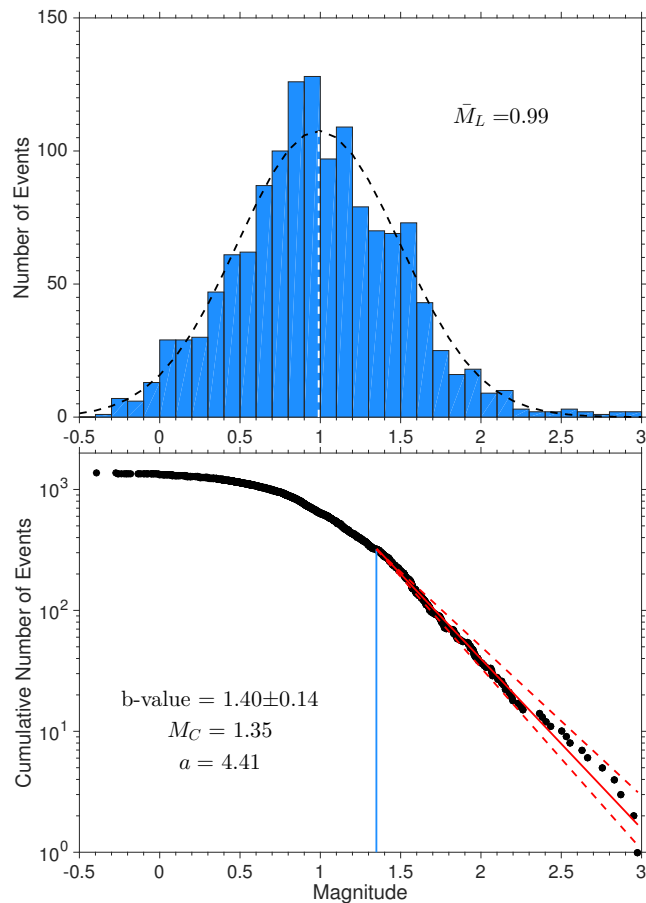


**Figure 5:** Distributions of earthquake magnitudes for 1361 earthquakes around Aluto. (top) Magnitude distributions plotted in 0.1 sized bins with a normal distribution also fitted. (bottom) The Gutenberg-Richter diagram for the events. b-values are solid red lines and the 95% confidence levels are red dashed lines. MC is the solid blue line.

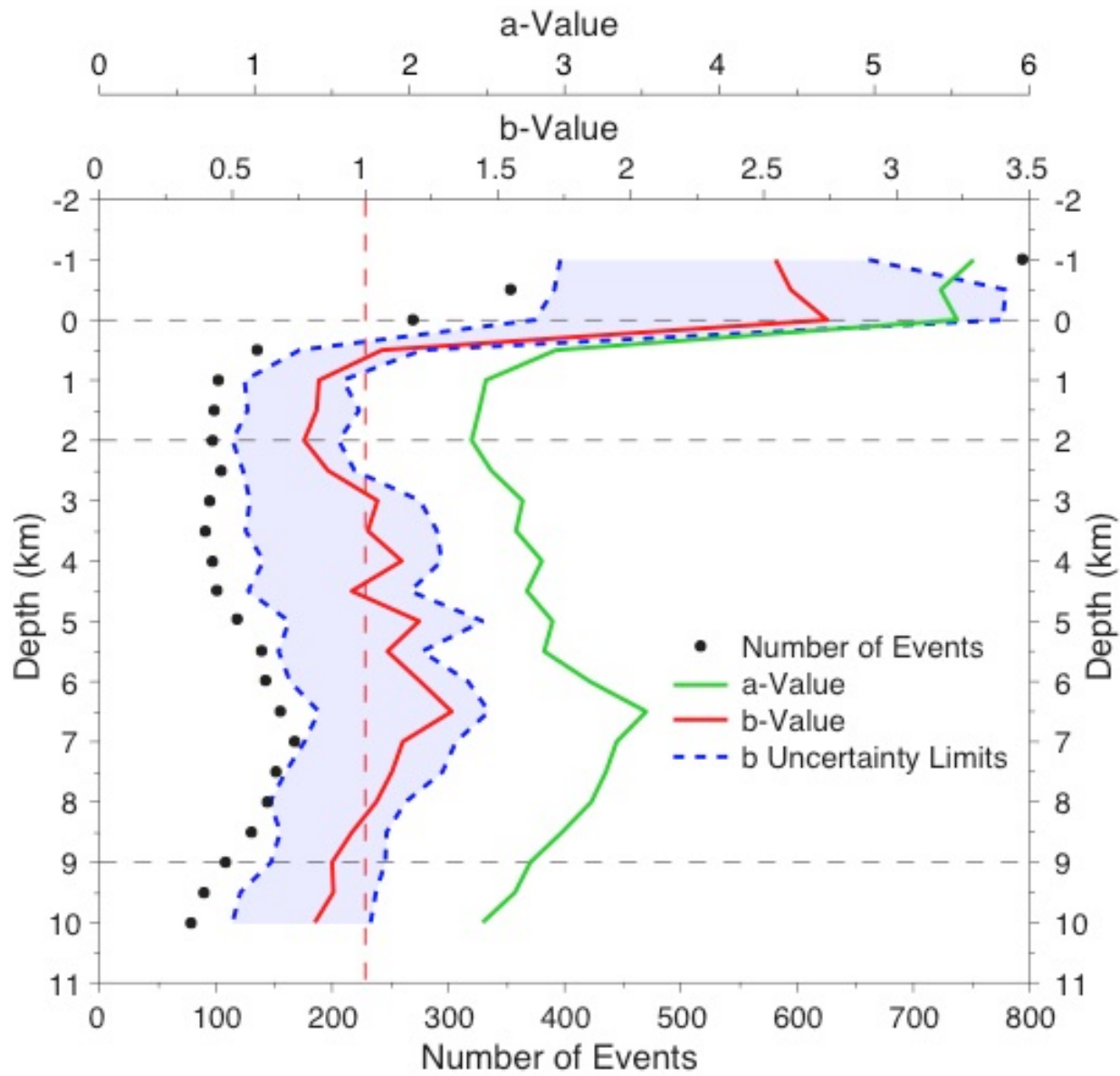


**Figure 6:** b-values plotted at increasing depth increments beneath Aluto. The calculated b-values (red line) and the associated upper and lower error bars (dashed blue lines) are plotted at the midpoint of the 2 km thick depth bins at 0.5 km spacings. The a-values are the green line, the number of events in each bin are the black circles and the tectonic average of  $\sim 1$  is the red dashed line.

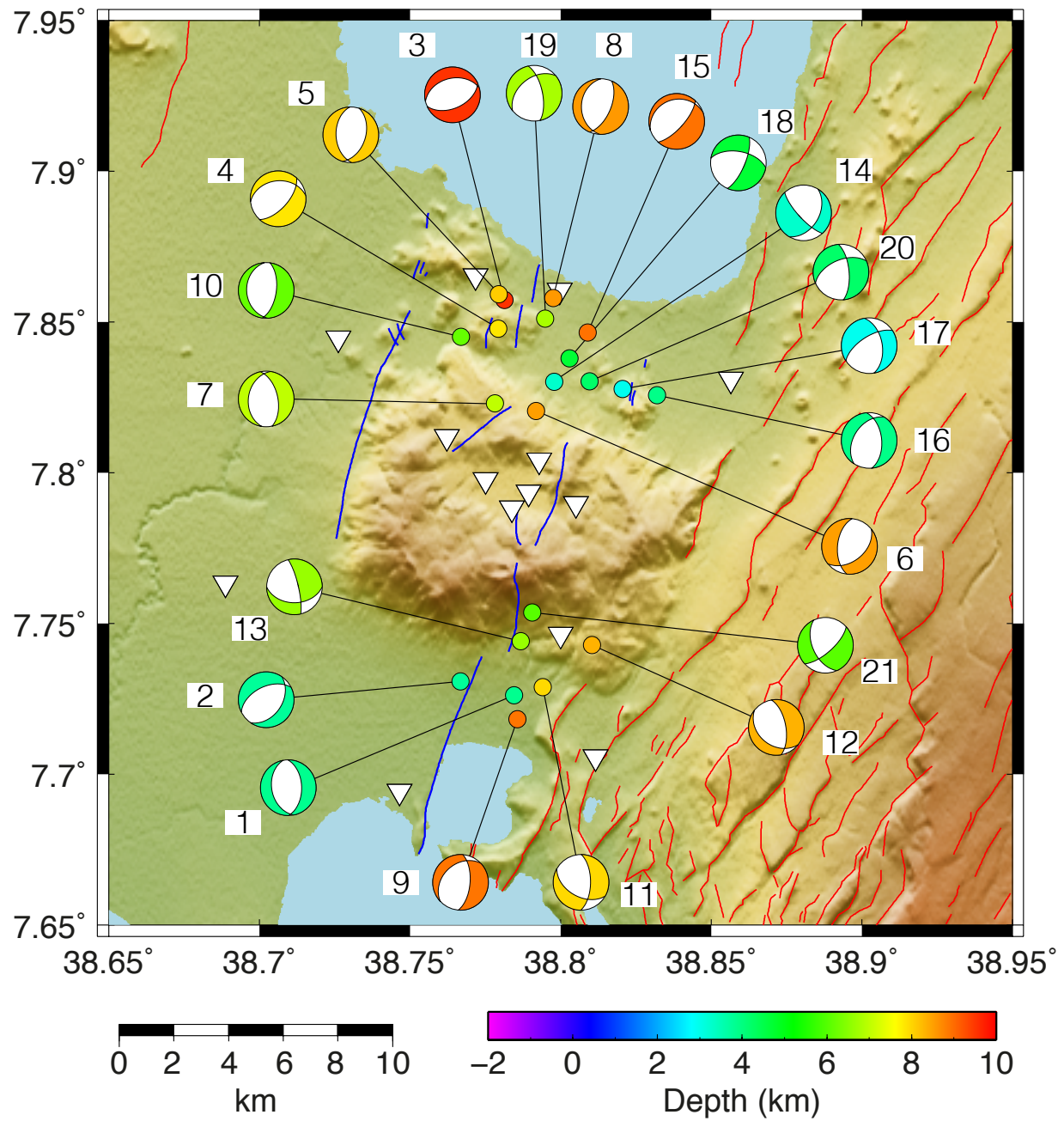


**Figure 7:** The 21 focal mechanisms computed around Aluto with dilatational quadrants coloured by depth. Border faults are red and the AJFZ and other faults of the Aluto complex are blue.

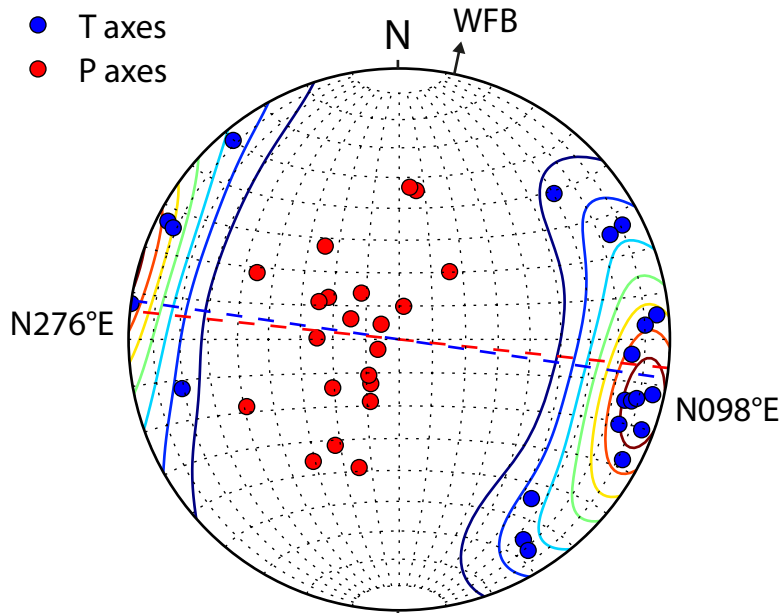


**Figure 8:** Lower hemisphere projections of the T- (blue) and P- (red) axes for 21 Aluto events. Dashed lines are the circular means of the axes azimuths and contours mark the density distribution of the T-axes.

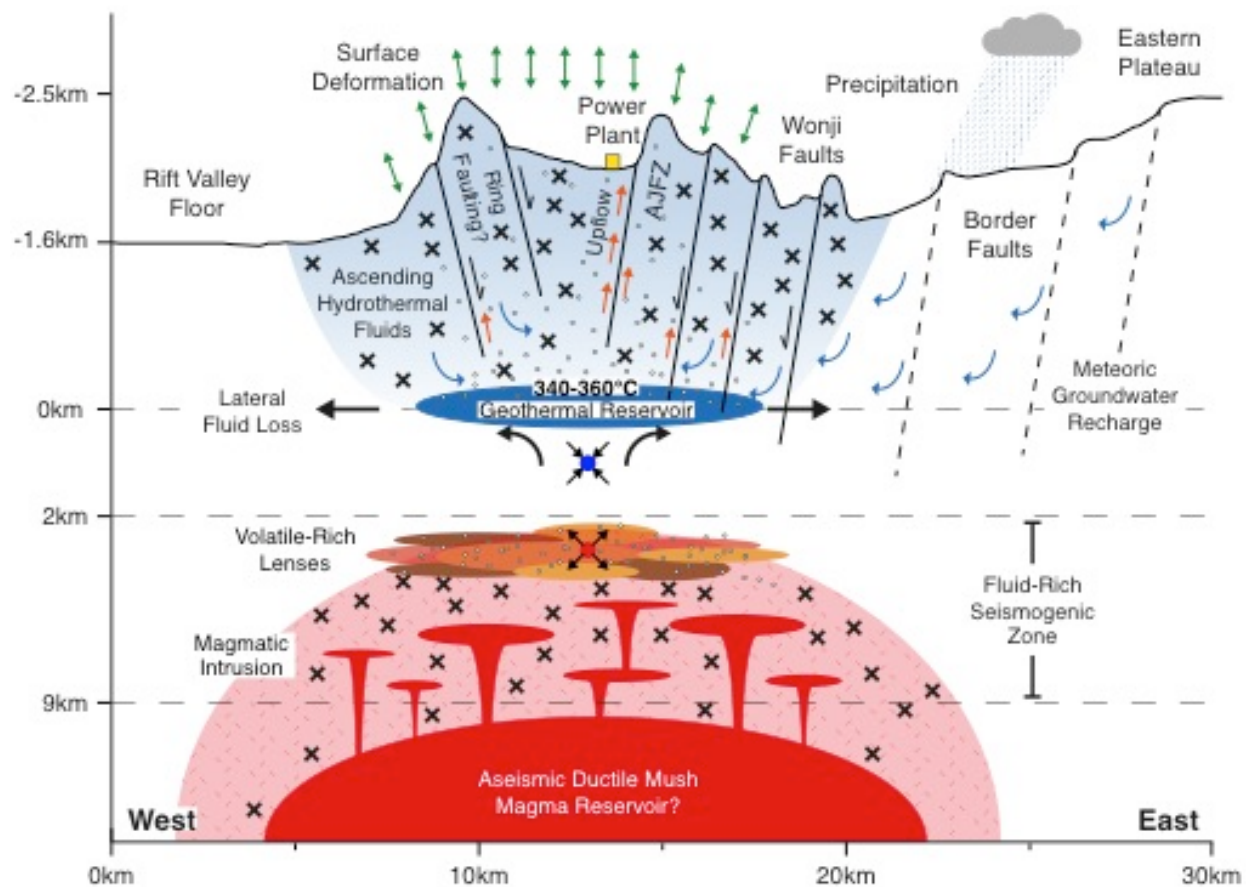


**Figure 9:** A schematic cross-section of the hydrothermal and magmatic systems beneath Aluto. An underlying ductile magmatic mush from which, magma intrudes into the region above it, generating seismicity and elevated b-values. Intrusion into a volatile- rich cap causes the exsolution of gases that drive periods of inflation at the surface. During periods of prolonged deflation, heat and volatile transfer is suppressed and little seismicity occurs between the

magmatic and geothermal reservoirs as the volatile cap seals quickly. The large temperature gradients across the geothermal reservoir circulate subsurface hydrothermal fluids within and above it, with the AJFZ providing the primary pathway of ascent. The reservoir is replenished by rainfall that upon heating circulates energetically and induces seismicity at shallow depths. Conversely, the border faults to the east remain relatively inactive, with the majority of strain localising along the WFB. Note: the vertical axis is not to scale.

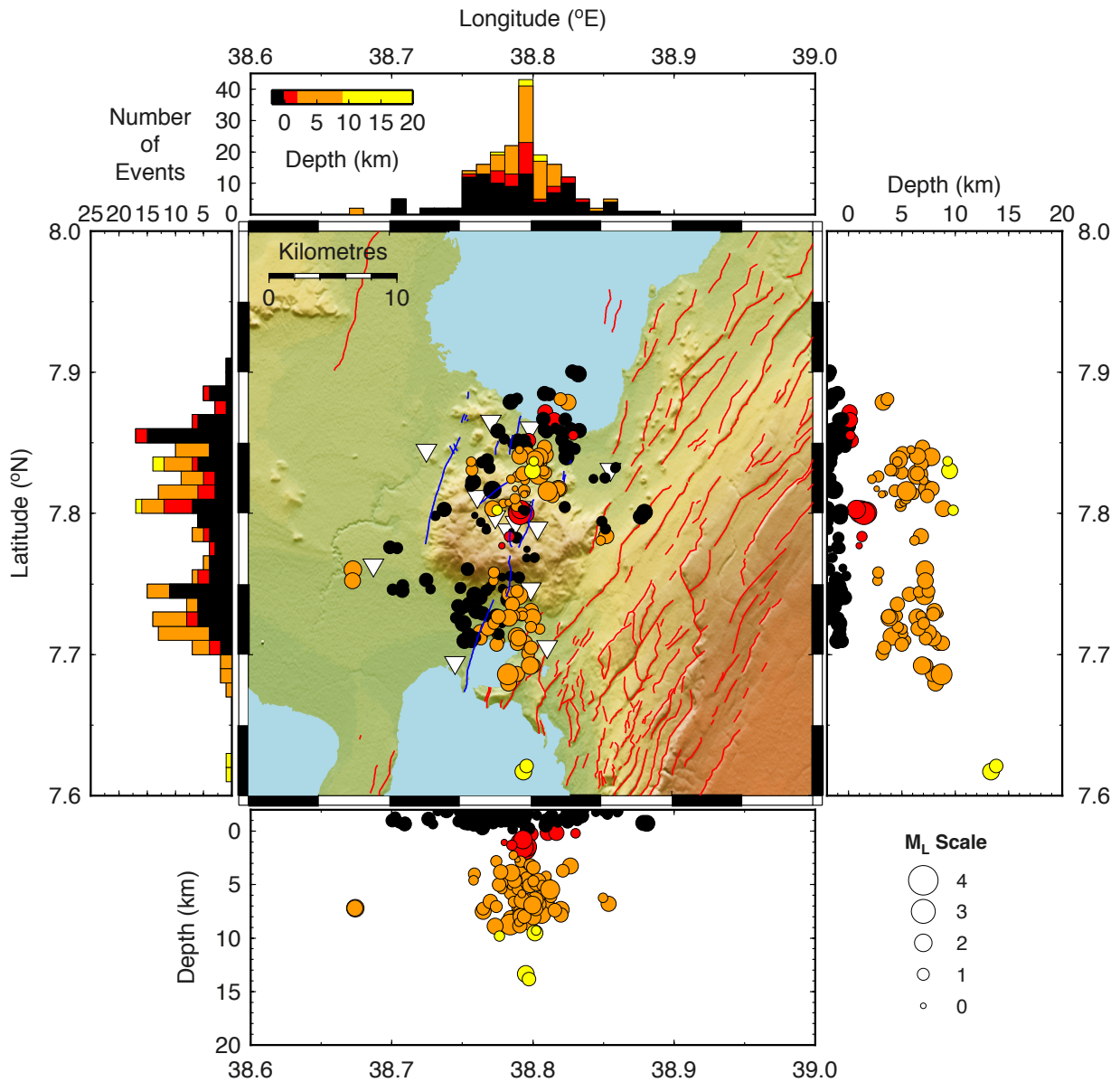


**Figure A.1:** The 218 double-differenced event locations around Aluto using *HypoDD*. Events are coloured by hypocentral depth into four depth sections and sized by local magnitude. Histograms with longitude and latitude are also presented.

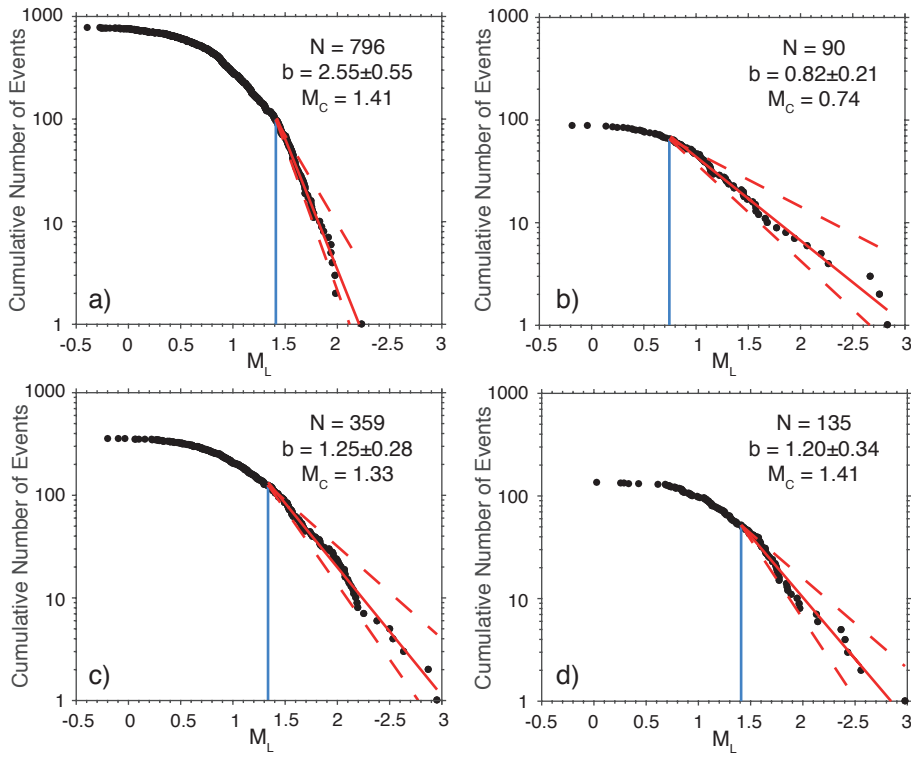


**Figure B.1:** Gutenberg-Richter distributions and b-value calculations for four depth ranges beneath Aluto: (a) above sea level, (b) between sea level and 2 km depth, (c) between 2 and 9 km and (d) below 9 km.

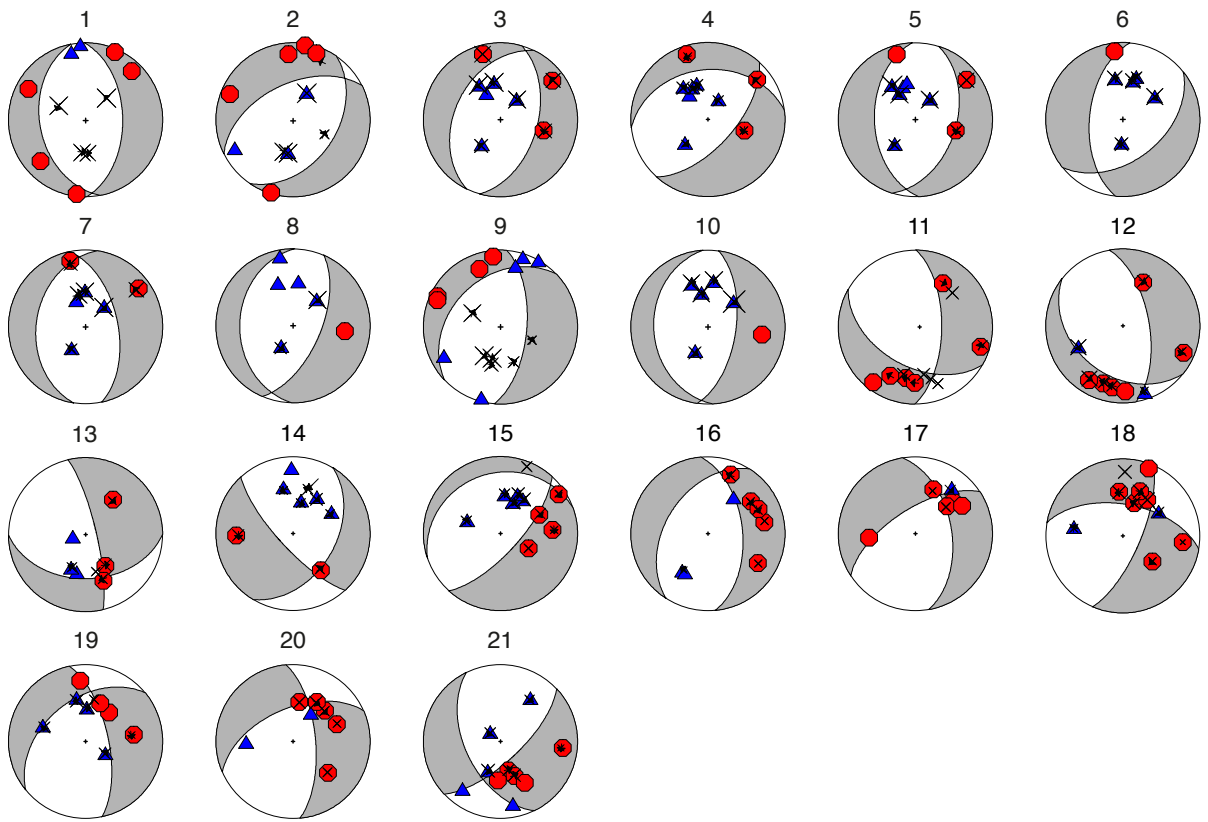


**Figure C.1:** Lower hemispherical projections of the 21 focal mechanisms at Aluto. Red octagons are compressional P-wave first-motions while blue triangles are dilatational. Arrows indicate the SH-first-motion directions. Amplitude ratios are crosses and sized by magnitude.

ID	Date	Time	Lat (°N)	Lat (°N)	Dep (km)	M <sub>L</sub>	Az Gap (°)	N	Dip (°)	Strike (°)	Rake (°)	P-Wave Pols	SH-Wave Pols	Amp Ratios	RMS Error
<b>1</b>	120117	02:28:12.137	7.726	38.785	3.86	1.8	126	36	50.18±5.90	359.18±21.70	-83.48	7/7	3/4	7/9	0.30
<b>2</b>	120430	01:24:05.369	7.731	38.767	3.77	1.6	145	6	51.62±2.08	243.68±2.86	-70.72	8/8	3/3	11/12	0.32
<b>3</b>	120625	07:04:26.045	7.857	38.782	9.53	3.0	113	1	40.26±0.00	205.93±0.00	-82.25	8/8	6/7	20/21	0.36
<b>4</b>	120625	07:05:22.611	7.848	38.779	7.84	2.9	118	3	35.53±1.95	263.58±2.35	-53.95	9/9	7/8	17/21	0.25
<b>5</b>	120625	12:30:53.481	7.859	38.780	8.08	3.0	116	5	45.86±2.65	17.46±51.50	-76.00	9/9	5/6	14/17	0.34
<b>6</b>	120625	12:39:29.379	7.821	38.792	8.50	1.9	170	32	46.03±4.20	51.66±36.43	-54.04	6/6	4/5	15/15	0.24
<b>7</b>	120625	13:16:20.426	7.823	38.778	7.00	2.0	159	4	36.22±1.76	188.86±3.12	-72.91	7/7	5/6	16/16	0.27
<b>8</b>	120820	20:51:07.549	7.858	38.798	8.57	1.3	135	39	60.50±4.79	23.47±9.06	-78.49	6/6	2/2	6/6	0.19
<b>9</b>	120924	22:07:37.458	7.718	38.786	8.90	2.2	176	1	35.53±0.00	226.52±0.00	-53.95	9/9	6/6	16/16	0.33
<b>10</b>	121001	21:12:30.669	7.845	38.767	6.15	1.5	136	33	60.13±16.28	7.88±55.53	-84.23	6/6	5/5	15/15	0.26
<b>11</b>	121211	23:33:52.714	7.729	38.794	7.96	1.3	138	2	61.98±0.88	0.53±0.68	-49.48	6/6	5/5	12/12	0.31
<b>12</b>	120217	05:31:34.960	7.743	38.811	8.32	2.3	140	11	61.98±12.44	349.99±49.18	-67.20	8/8	6/7	8/9	0.35
<b>13</b>	120723	02:01:04.324	7.744	38.787	6.63	0.9	138	2	78.56±2.95	346.86±3.24	-49.02	6/6	3/4	3/4	0.30
<b>14</b>	120803	18:39:58.390	7.830	38.798	3.28	1.6	126	6	43.96±17.11	31.03±54.14	-22.18	8/8	6/7	17/18	0.36
<b>15</b>	120825	15:04:02.665	7.847	38.809	8.93	2.6	171	3	22.27±7.09	251.14±64.52	-62.73	9/9	8/8	25/27	0.32
<b>16</b>	131016	00:10:21.490	7.826	38.832	3.92	0.8	135	4	43.96±1.58	212.76±11.29	-60.48	8/8	3/4	16/17	0.33
<b>17</b>	131016	00:23:50.055	7.828	38.821	2.95	0.3	137	6	63.94±16.38	236.96±52.12	-44.31	6/6	1/1	3/4	0.35
<b>18</b>	131025	11:37:18.850	7.838	38.803	4.70	2.0	146	2	56.17±1.25	219.95±2.15	-22.76	9/9	5/6	17/22	0.32
<b>19</b>	131211	00:07:38.704	7.851	38.795	6.78	1.1	167	1	44.81±0.00	230.91±0.00	-35.53	8/8	4/5	11/14	0.39
<b>20</b>	131212	01:00:48.491	7.830	38.810	4.22	0.8	136	2	54.60±4.69	246.46±42.49	-29.84	7/7	2/2	8/9	0.39
<b>21</b>	131214	00:16:08.242	7.754	38.791	6.03	1.4	189	5	69.30±5.18	46.91±8.19	-40.89	10/10	6/6	15/16	0.33

**Table C.1:** Focal mechanism parameters output from *FOCMEC* for the 21 earthquakes around Aluto. N is the number of possible solutions. Dip and strike uncertainties are the circular standard deviations of the possible solutions. The RMS error is for the amplitude ratios of the accepted solution.